On the Performance of Fuel Elements Enriched in the SOLASE-H Hybrid Reactor

R.M. Lewis, P.R. Schwab, and W.G. Wolfer

February 1980

UWFDM-324

FUSION TECHNOLOGY INSTITUTE

UNIVERSITY OF WISCONSIN

MADISON WISCONSIN

On the Performance of Fuel Elements Enriched in the SOLASE-H Hybrid Reactor

R.M. Lewis, P.R. Schwab, and W.G. Wolfer

Fusion Technology Institute
University of Wisconsin
1500 Engineering Drive
Madison, WI 53706

http://fti.neep.wisc.edu

February 1980

UWFDM-324

"LEGAL NOTICE"

"This work was prepared by the University of Wisconsin as an account of work sponsored by the Electric Power Research Institute, Inc. ("EPRI"). Neither EPRI, members of EPRI, the University of Wisconsin, nor any person acting on behalf of either:

"a. Makes any warranty or representation, express or implied, with respect to the accuracy, completeness, or usefulness of the information contained in this report, or that the use of any information, apparatus, method, or process disclosed in this report may not infringe privately owned rights; or

"b. Assumes any liabilities with respect to the use of, or for damages resulting from the use of, any information, apparatus, method or process disclosed in this report."

On the Performance of Fuel Elements Enriched in the SOLASE-H Hybrid Reactor

R.M. Lewis

P.R. Schwab

W.G. Wolfer

Fusion Engineering Program
Nuclear Engineering Department
University of Wisconsin
Madison WI 53706 U.S.A.

UWFDM-324

February 1980

Content

Summary

Several problems related to the direct enrichment of LWR (light water reactor) fuel assemblies in a laser fusion hybrid reactor, SOLASE-H, are examined. These problems are:

a) the generation of a thermoelastic shock wave in the fuel due to the pulsed nature of the fusion neutron flux;
b) the thermal cycling of the fuel due to the intermittent power generation in the fuel assembly;
c) the bowing of the fuel elements and the fuel assembly due to the neutron flux and temperature gradients in the blanket zone;
d) the compatibility of zircaloy as a cladding material with sodium used as a coolant in the fusion hybrid;
e) the adequacy of present day sodium removal procedures for cleaning the LWR fuel assemblies.

The answers to these problems can be summarized as follows:

a) The amplitude of the thermoelastic stress wave is very small in the SOLASE-H hybrid reactor. The reason is to be found in the lack of neutron moderation, and hence, the low power production.

The alternative strategy to avoid shock heating by spreading out the neutron pulse time is self-defeating, because it would require substantial neutron moderation. This in turn would greatly increase the power production.

b) The intermittent heating and cooling of the fuel pellets can be avoided by using oxide fuel which has a low thermal conductivity in comparison to carbide or metallic fuel. Cyclic cracking of the fuel pellets is thereby prevented.

c) Bowing due to differential swelling in the fuel elements and fuel assembly during enrichment in SOLASE-H is comparable to bowing in present-day LWRs. Using very conservative assumptions it is found that the pull force necessary to extract a bowed fuel assembly from the blanket zone is no larger than the weight of the assembly.

d) The compatibility of zircaloy with sodium is governed by the oxygen content in the coolant. Negligible corrosion of zircaloy results when the oxygen is kept below 5 ppm. This can be achieved with available trapping technology.

e) Effective sodium removal from the enriched LWR fuel assembly is important in order to avoid stress-corrosion cracking in the water environment of the LWR. The current sodium removal process with a steam-argon mixture is judged adequate. However, should current research prove the evaporative process feasible, it should be preferred.

The positive answers to the problems examined indicate that direct enrichment of LWR fuel assembly in the SOLASE-H reactor is a viable concept.

I. Introduction

In the SOLASE-H laser fusion hybrid design[1], the possibility was studied to directly enrich light water reactor (LWR) fuel assemblies with fissile isotopes.

In order to reach the 4% enriched fuel necessary for LWR operation, the fuel assemblies must reside in the fusion hybrid reactor for about two and a half years. During this time, the cladding material accumulates a radiation damage dosage of about 20 dpa*. In comparison, the displacement damage in the LWR is only a few dpa for the residence time of the fuel assemblies.

A further, and important difference exists for the fuel burn-up in the fusion hybrid and the thermal reactor. Whereas the power production of a fuel element in a LWR is typically from 15 to 25 kW/m, the maximum linear power of a fuel element is only 4.43 kW/m in the SOLASE-H blanket at the end of the enrichment cycle. This low value is due to the absence of a large thermal neutron spectrum component in the blanket region of the SOLASE-H reactor. We note that in other hybrid design studies, substantial neutron moderation and high power production was considered desirable. However, from the point of view of fuel element performance, a low power production is more desirable for enrichment in a laser fusion hybrid. This is connected with the pulsed nature of the neutron irradiation in any inertial fusion reactor. Pulsed irradiation produces temperature cycling in the fuel elements with a possible generation of thermo-elastic waves and thermal ratcheting effects. These problems will be assessed in more detail in Sections III and IV.

---

*dpa (displacements per atom) is a unit for accumulated radiation damage. 1 dpa means that during the exposure each atom in the solid has become dislodged once due to energetic recoils.

A major concern of the direct enrichment scheme with LWR fuel assemblies is the effect of the radiation damage to the fuel element performance. Unfortunately, there are no irradiation experiments on LWR fuel elements in which a radiation damage level has been reached that approaches the one in SOLASE-H or any other fusion hybrid. However, a situation closest to the one considered here is realized in fission breeder reactors, specifically in liquid metal fast breeder reactors (LMFBR). Here, extensive irradiation experience on fuel assemblies and fuel elements has been accumulated over the years, with radiation damage levels to the cladding up to 100 dpa.

Fig. I.1 and Fig. I.2 summarize the French experience[2] up to the year 1977.

As there are 61 fuel elements in Rapsodie assemblies, and 217 for the Phénix fuel assemblies, the total number of irradiated fuel pins amounts to 66,000 in the French breeder program. A similar experience exists in the British breeder program and, to a lesser extent, in the U.S. breeder program. Based on this experience, there can be little doubt that a target exposure of 120 dpa can easily be reached for the cladding of a commercial fast breeder reactor. The cladding materials considered for LMFBRs are almost exclusively austenitic stainless steels. New alloys and ferritic steels are, however, part of the more recent alloy development programs.

According to the scant information available on the radiation-induced swelling in other cladding materials and in Zircaloys it appears that the austenitic stainless steels are among the most swelling-prone structural materials for in-core applications, and that swelling is almost certainly less in zirconium-based alloys.

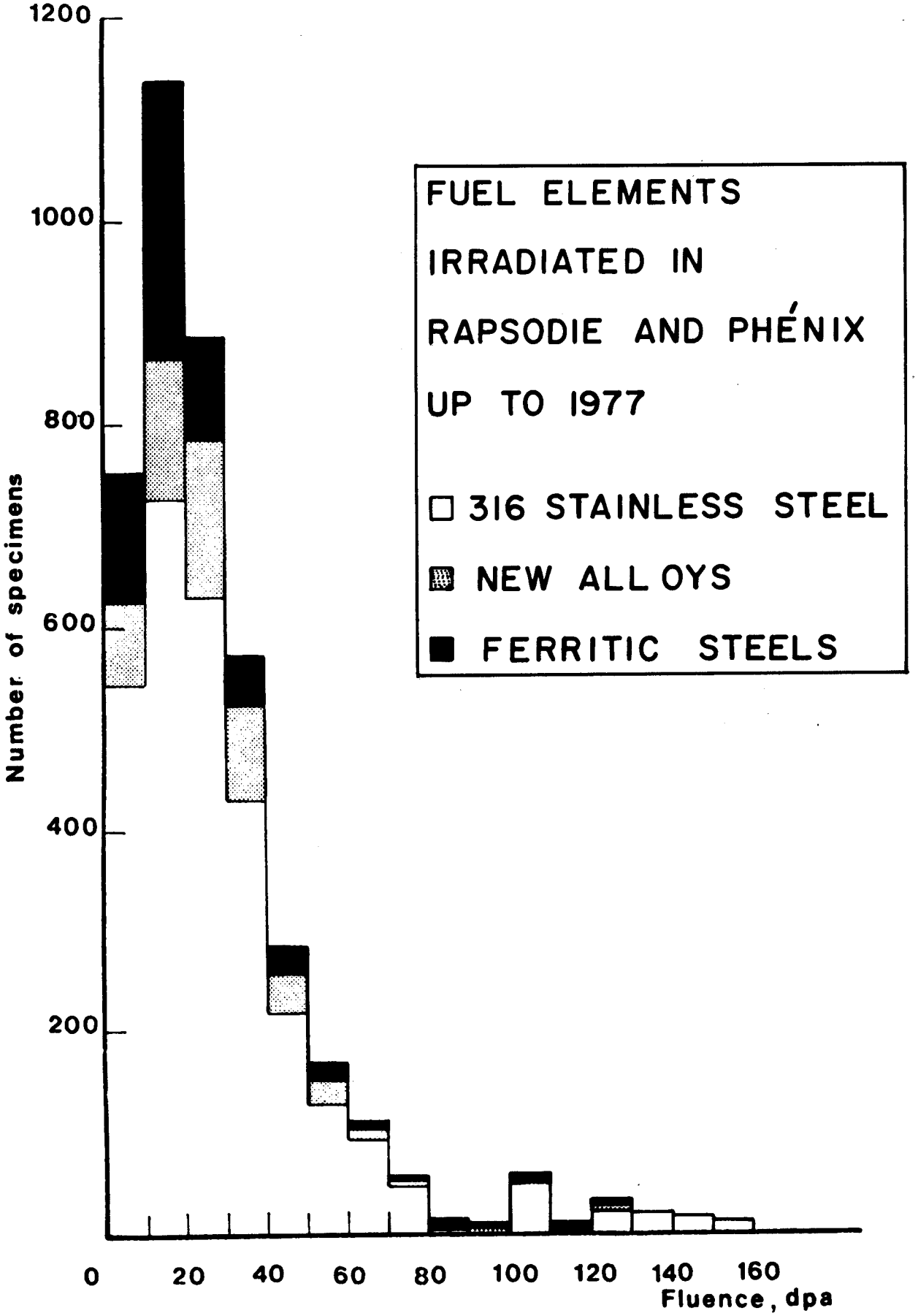

Fig. I.1. Number of Fuel Elements Irradiated in the French LMFBR Program to a Given Fluence.

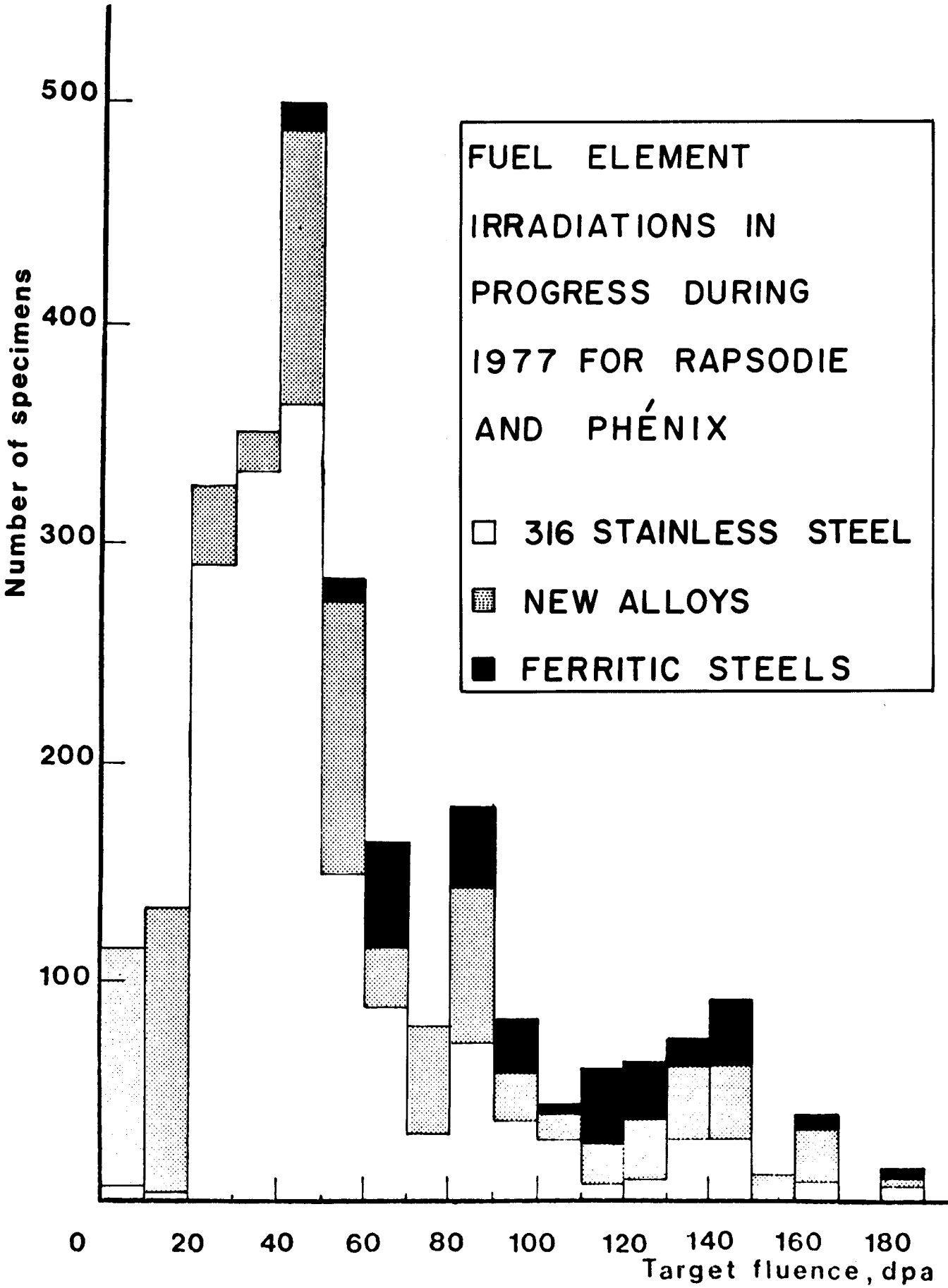

Fig. I.2. Number of Fuel Elements to be Irradiated to a Given Target Fluence.

It then seems reasonable to proceed on the following assumption with regard to fuel element performance in a direct enrichment scheme.

If fuel elements, clad in austenitic stainless steels, perform well in the fusion hybrid and the LWR environments, elements clad in Zircaloys should perform equally well or even better, provided there are no problems with regard to compatibility of coolant and cladding, or other effects specific to Zircaloys.

Adopting this philosophy, we have assumed that the fuel element cladding is type 316 stainless steel whenever an assessment has to be made with regard to radiation damage. In this report, this assumption is used only in the context of fuel element bowing. This subject is treated in Section V.

In order to avoid neutron moderation in the fusion hybrid SOLASE-H, sodium was chosen as a coolant rather than water. Accordingly, compatibility between Zircaloy and sodium becomes an important consideration, and Section VI provides a critical assessment of the pertinent data.

The transfer of the enriched fuel assemblies to the LWR requires that they can be cleaned completely of sodium prior to the insertion in the core of a LWR. Any sodium residue trapped in crevices or incipient cracks would react with the water and cause stress corrosion and further crack propagation in addition to adversely affecting the coolant water chemistry in the primary circuit of the LWR.

Therefore, an extensive review was carried out on the effectiveness of sodium removal procedures which is summarized in Section VI.

In the following Section II, a brief description of the blanket zone of the fusion hybrid SOLASE-H is given together with the power, temperature, and the radiation damage distributions.

II. The Blanket Zone

The reactor cavity of SOLASE-H is cylindrical with dome-shaped end-zones, as shown in Fig. II.1. The blanket zone is behind the first wall and a lead-containing zone for neutron multiplication. The annular blanket zone has a height of 12 m so that three standard LWR fuel assemblies can be arranged vertically. The sodium coolant flows through all three fuel assemblies with the inlet being at the bottom. As described in Ref. 1, the fuel assemblies will be shuffled and rotated during the enrichment period in order to minimize both the axial and radial fissile isotope gradients.

The power distribution within the fuel assemblies varies axially as well as radially. The shape of the axial power distribution is shown in Fig. II.2, whereas the radial power distribution in the midplane of the reactor cavity is illustrated in Fig. II.3. These distributions are based on a uniform fissile material distribution, and they approximate the actual power distribution to within 10% at any given time during the enrichment cycle. The sodium coolant temperature distribution in the axial direction is shown in Fig. II.4.

The neutron displacement damage rate in the cladding, being proportional to the neutron flux, exhibits also an axial and radial dependence. Fig. II.5 shows the radial dependence through the blanket zone in the midplane for both Zircaloy and type 316 stainless steel. The axial dependence can simply be scaled according to the axial power profile shown in Fig. II.2.

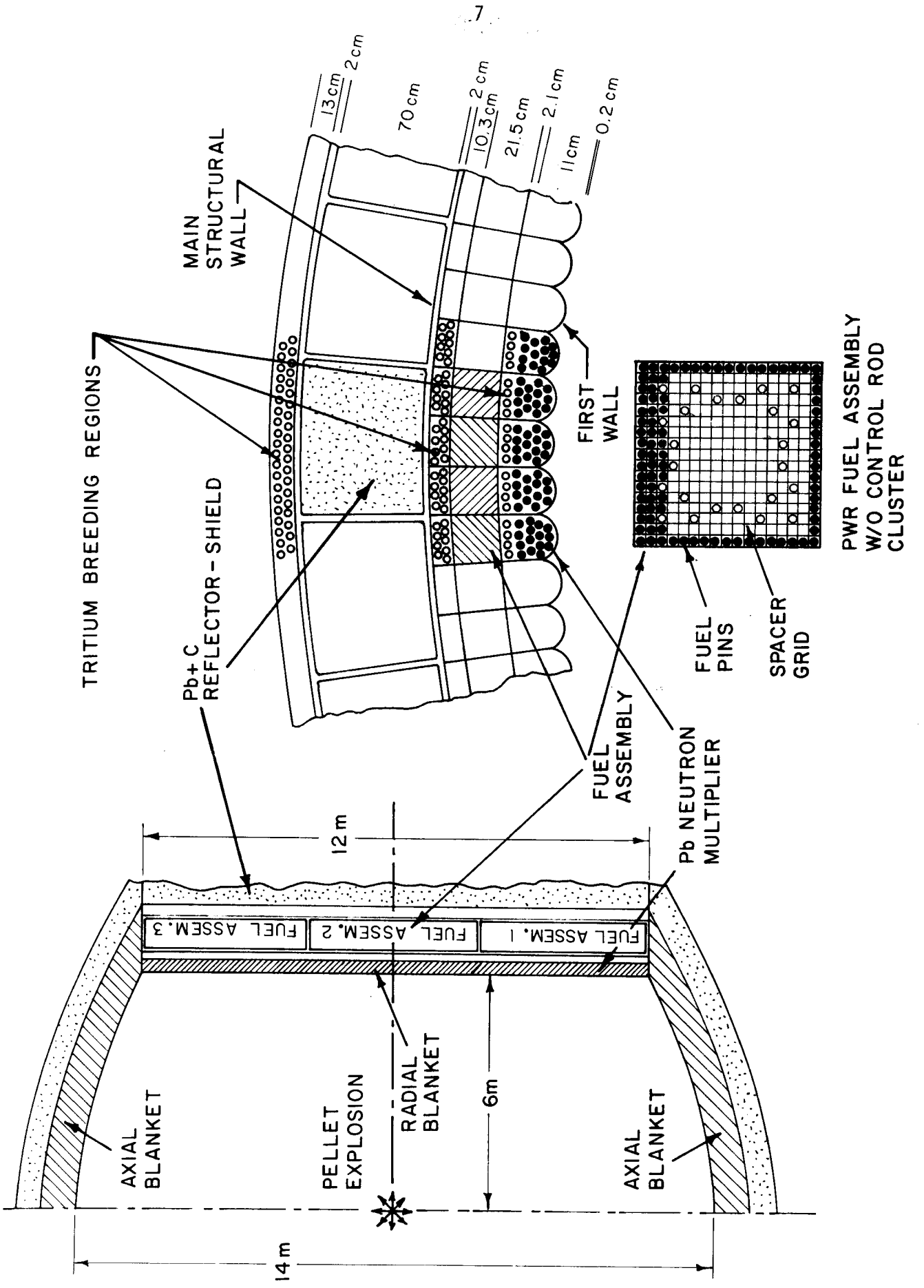
TRITIUM BREEDING REGIONS
MAIN STRUCTURAL WALL
Pb+C REFLECTOR-SHIELD
FIRST WALL
FUEL ASSEMBLY
Pb NEUTRON MULTIPLIER
FUEL PINS
SPACER GRID
PWR FUEL ASSEMBLY W/O CONTROL ROD CLUSTER
13 cm
2 cm
70 cm
2 cm
10.3 cm
21.5 cm
2.1 cm
11 cm
0.2 cm
12 m
FUEL ASSEM. 1
FUEL ASSEM. 2
FUEL ASSEM. 3
AXIAL BLANKET
PELLET EXPLOSION
RADIAL BLANKET
6m
AXIAL BLANKET
14 m

Fig. II.1

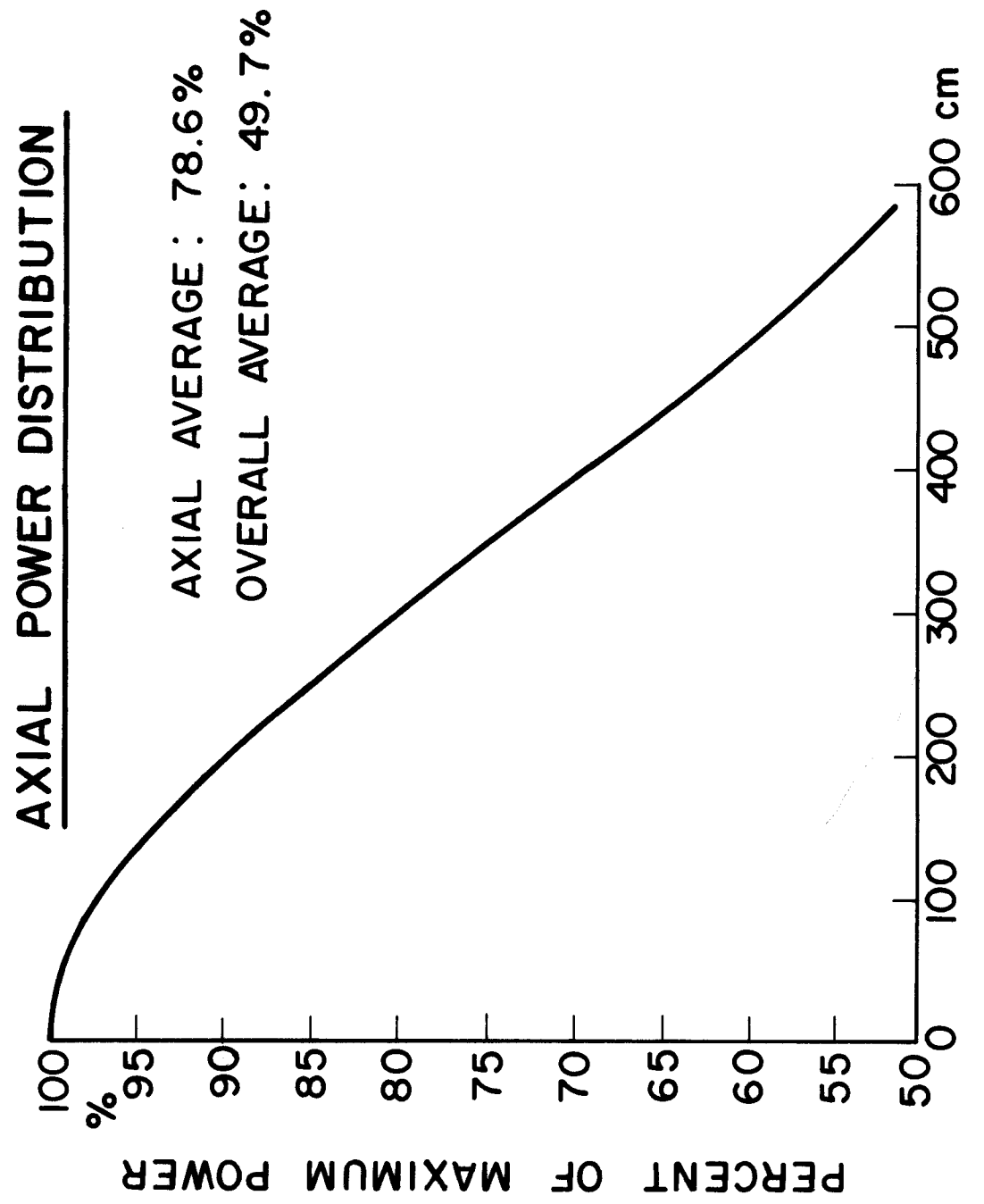
AXIAL POWER DISTRIBUTION
AXIAL AVERAGE : 78.6%
OVERALL AVERAGE: 49.7%
PERCENT OF MAXIMUM POWER
100
%
95
90
85
80
75
70
65
60
55
50
0
100
200
300
400
500
600 cm
AXIAL DISTANCE FROM MIDPLANE

Figure II.2

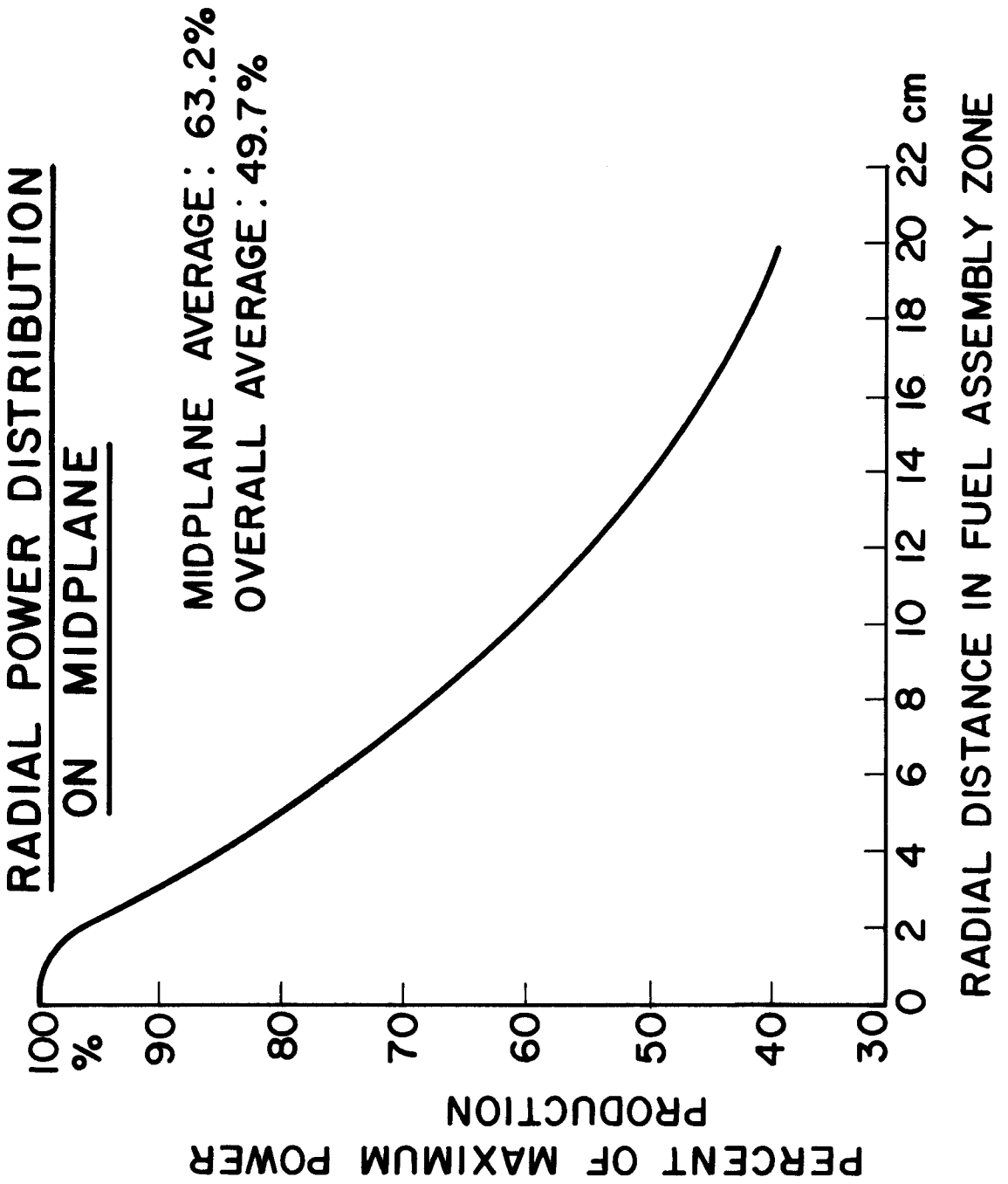
RADIAL POWER DISTRIBUTION
ON MIDPLANE
MIDPLANE AVERAGE: 63.2%
OVERALL AVERAGE: 49.7%
PERCENT OF MAXIMUM POWER PRODUCTION
100 %
90
80
70
60
50
40
30
0 2 4 6 8 10 12 14 16 18 20 22 cm
RADIAL DISTANCE IN FUEL ASSEMBLY ZONE

Figure II.3

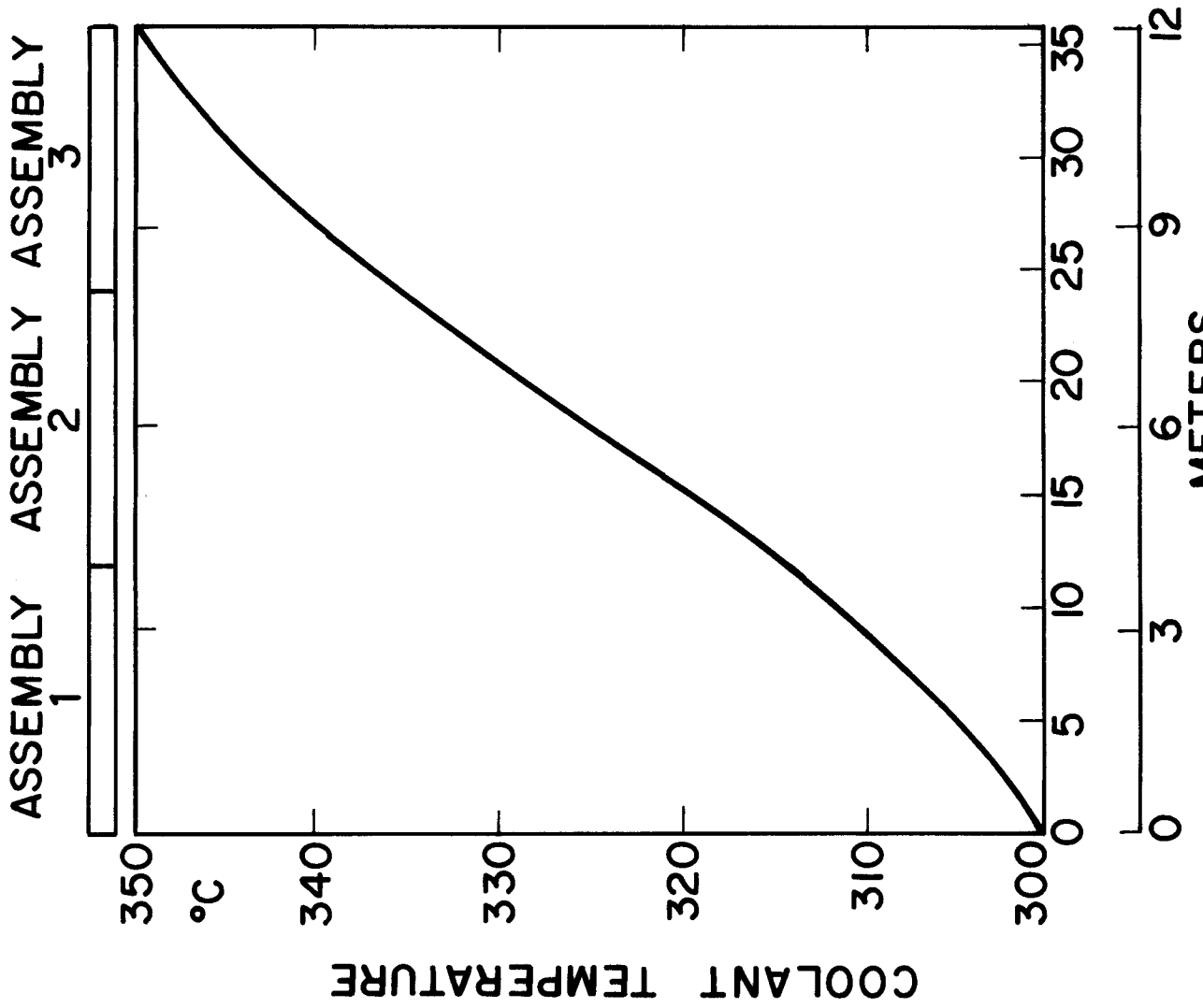
ASSEMBLY 1
ASSEMBLY 2
ASSEMBLY 3
COOLANT TEMPERATURE
°C
350
340
330
320
310
300
0
5
10
15
20
25
30
35
0
3
6
9
12
METERS

Figure II.4

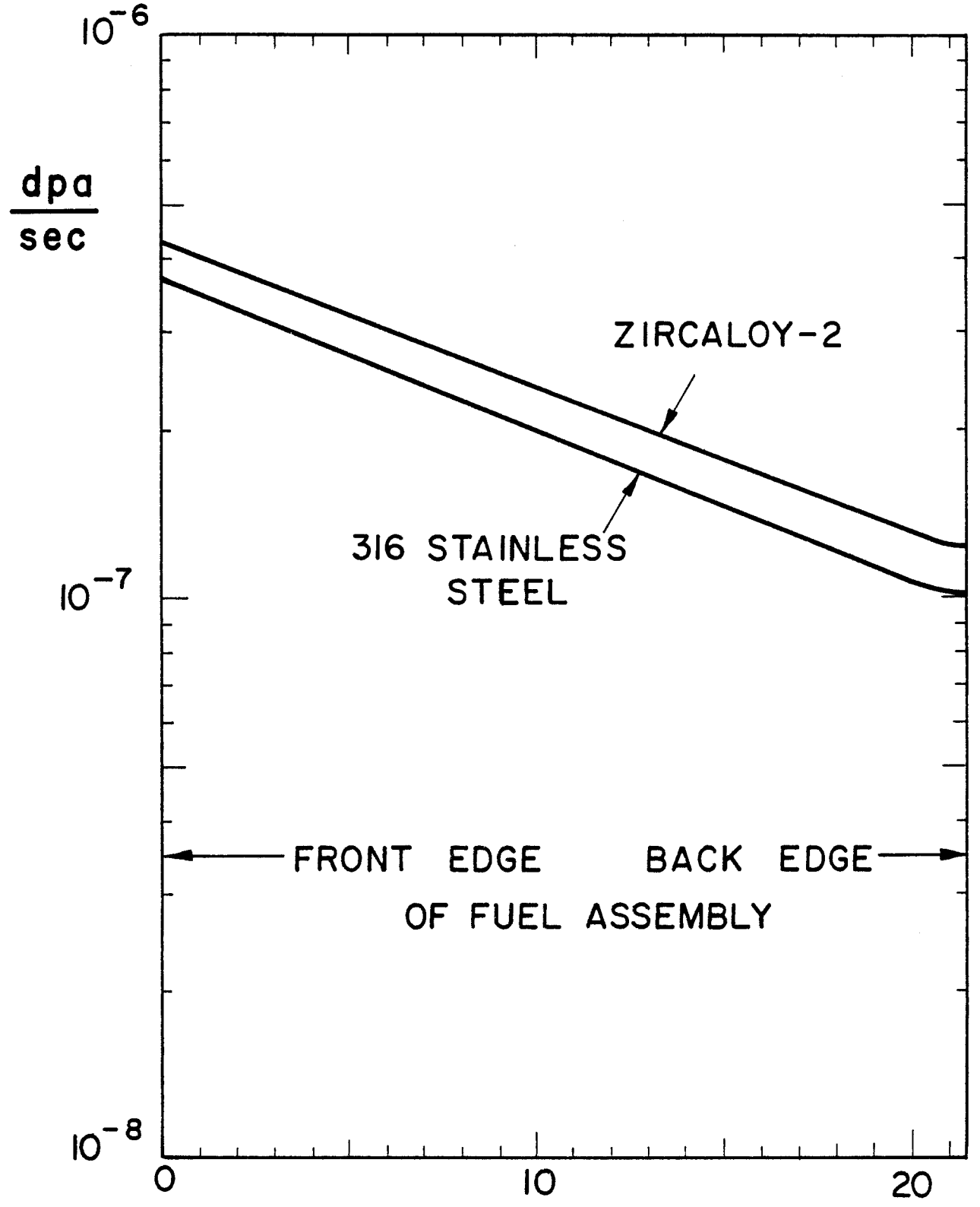

Displacement Damage in dpa

Figure II.5

If a fuel assembly were to reside axially in the middle position at all times, and if it were not rotated, the fuel element closest to the front edge would receive on the midplane a total exposure of 36.2 dpa (for Zircaloy) or 31.5 dpa (for SS316) during the enrichment period of 2.7 years. In reality, because of the shuffling and rotating procedure, the average displacement damage in the cladding is less by about a factor of two, with an estimated variation of about 10% across the fuel assembly. We note that this variation is less than the uncertainty associated with the basic models for displacement computations, and substantially less than the scatter in most radiation effects data.

III. Thermoelastic Shock Wave

Due to the pulsed nature of the neutron production in SOLASE-H or any other fusion reactor based on inertial confinement, the fission rate in the fuel is also pulsed. The intermittent heat generation may cause a thermoelastic shock wave to spread across the fuel pellet. Upon reflection at the boundary of the pellet, spallation may disintegrate the fuel pellet, and debris may impact on the cladding. A similar momentum transfer in axial direction may push fuel pellets in the plenum region, and/or may create gaps in the fuel stack. When returned to the LWR, these fuel elements may be subject to the clad collapse mechanism with subsequent fuel element failure. Therefore, the generation of a thermoelastic shock wave of substantial amplitude must be averted in any fusion hybrid enrichment scheme.

An assessment of this problem in the following will demonstrate that the thermoelastic shock wave produced during one neutron pulse within a fuel element in the blanket region of SOLASE-H is indeed very small, and no adverse effects on the fuel or the cladding integrity should result from the pulsed neutron irradiation. The reason for this favorable result is that the power generation during one neutron pulse is sufficiently small to give a temperature increase of only a few degrees. It will also become evident that high power production in the fuel elements can only be tolerated if the neutron pulse width is broadened in time to be of the order of 100 μs or longer. This can only be accomplished through substantial energy moderation of the original neutron pulse which results in further increase of the power production.

Therefore, this causative cycle of thermoelastic shock wave generation and power production can best be broken by avoiding neutron moderation.

It is not necessary for the following assessment of this problem to perform a detailed analysis, as simple calculations will suffice to obtain a good estimate of the amplitude of the thermoelastic shock wave.

We approximate the fuel pellet by a cubic solid of length L, and assume that the latter is heated so that the temperature changes uniformly according to a ramp function

$$T(t) = \begin{cases} T_0 & \text{for} \quad t \leq 0 \\ T_0 + \Delta T t/\tau_0 & \text{for } 0 \leq t \leq \tau_0 \\ T_0 + \Delta T & \text{for } t_0 \leq t \quad , \end{cases}$$

illustrated in Fig. III.1. The temperature rise time τ_0 is equal to the duration of the neutron pulse as it traverses the fuel element. If the rise time τ_0 is sufficiently short, mass inertia prevents a stress-free thermal expansion of the solid, and compressive stresses are created. These stresses set in motion a thermoelastic wave propagating from the boundary into the solid with the speed of sound

$$s = \sqrt{E/\rho} \quad , \tag{III.1}$$

where ρ is the density of the solid and E its Young's modulus.

After a transit time of the order of

$$\tau_1 = L/s \tag{III.2}$$

a tensile stress wave propagates through the solid.

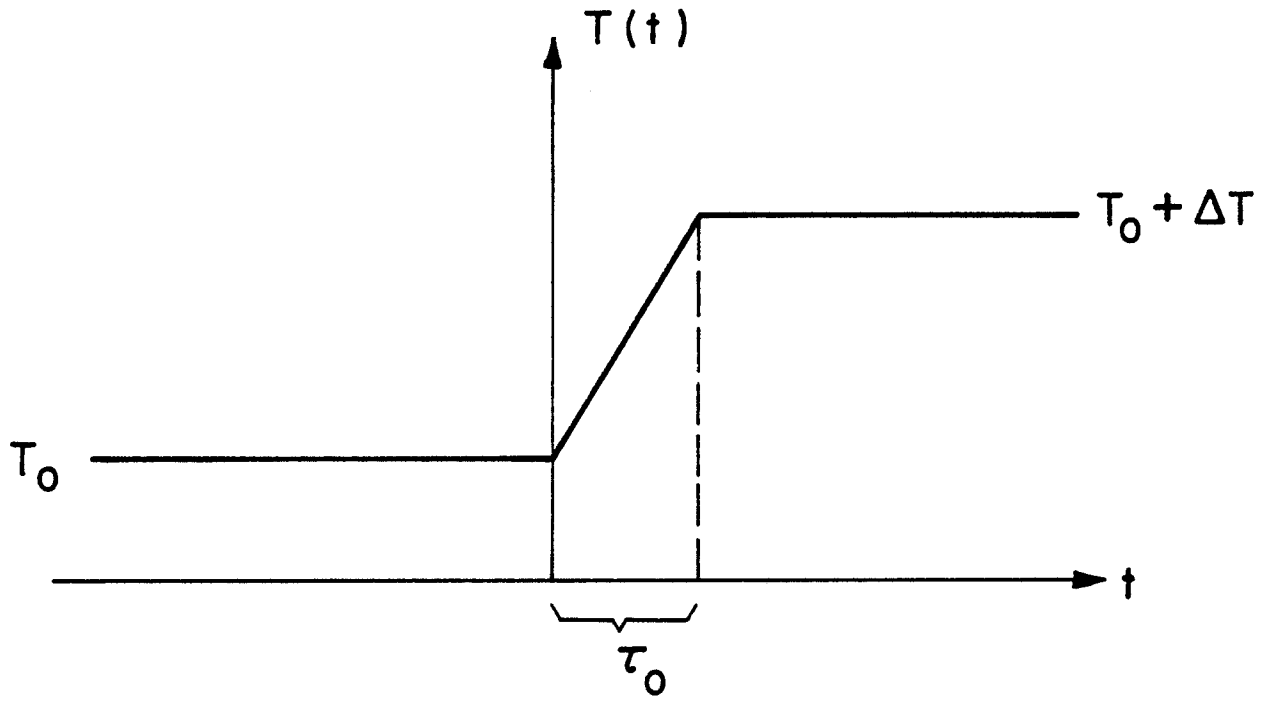

Fig. III.1. Schematic Temperature Rise in a Fuel Element Due to One Neutron Pulse.

The maximum (compressive or tensile) stress amplitude produced by the shock heating is given by

$$\frac{|\sigma_{max}|}{\alpha E \Delta T} = \begin{cases} 1 & \text{if } \tau_o \leq \tau_1 \\ \dfrac{\tau_1}{\tau_o} & \text{if } \tau_1 \leq \tau_o \end{cases} , \qquad \text{(III.3)}$$

where α is the linear thermal expansion coefficient.

The lower part of Eq. (III.3) demonstrates clearly that a thermal-elastic wave can be avoided entirely when the temperature rise time τ_o is much larger than the transit time τ_1 of the acoustic wave.

The dimensions of a LWR fuel pellet are 11.6 mm for the diameter and 13 mm for the height. The travel distance for the thermoelastic wave is about half of these values, or typically about 6 mm.

If we consider three types of fuel, metallic, carbides, and oxides, we find with the data listed in Table III.1, that the transit time τ_1 is about 2 μs regardless of the fuel type. This is substantially longer than the duration of the neutron pulse of about 10 ns, and therefore, τ_1 is also much longer than the temperature rise time τ_o associated with the fission power production. Hence, the upper part of Eq. (III.3) must be used, and the maximum stress amplitude is

$$|\sigma_{max}| = \alpha E \Delta T \quad . \qquad \text{(III.4)}$$

The temperature increase ΔT per neutron pulse can be estimated as follows. According to the heat conduction equation

$$\Delta T/\tau_o = \dot{Q}_m/c \quad , \qquad \text{(III.5)}$$

Table III.1

Fuel	U	Th	UC	ThO_2	UO_2
Density, ρ [kg/m^3]	1.94×10^4	1.17×10^4	1.4×10^4	1.0×10^4	1.1×10^4
Specific heat C [J/kg/°K]	410	305	230	243	247
Thermal expansion α[$°K^{-1}$]	4.6×10^{-5}	1.15×10^{-5}	1.05×10^{-5}	1.3×10^{-5}	1.2×10^{-5}
Elastic modulus E, [MPa]	1.66×10^5	7.3×10^4	2.17×10^5	1.38×10^5	1.72×10^5
Fracture stress [MPa]	386	214	75	70	70
Speed of sound [m/s]	2930	2500	3950	3710	3970
Transit time τ_1 [s]	2.05×10^{-6}	2.4×10^{-6}	1.5×10^{-6}	1.6×10^{-6}	1.5×10^{-6}
Thermal diffusivity [m^2/s]	4.07×10^{-6}	1.27×10^{-5}	7.2×10^{-6}	1.3×10^{-6}	7.8×10^{-7}
Temperature rise ΔT [°K]	1.28	2.84	3.17	4.17	3.76
Stress amplitude σ_{max} [MPa]	9.8	2.4	7.2	7.5	7.8

where c is the specific heat of the fuel and $\dot{Q}_m$ the average heating rate per unit mass. We may express $\dot{Q}_m$ in terms of the time-averaged heat flux q leaving the fuel pin by

$$\dot{Q}_m = 2q/(n\tau_o \rho r) \qquad \text{(III.6)}$$

where 2r is the fuel element diameter and n the number of neutron pulses per second.

In SOLASE-H, n was selected to be equal to four. The heat flux q increases with the irradiation time, and it reaches a maximum value of $q_o = 12.16\ W/cm^2$ at the end of the enrichment cycle. Therefore, the maximum value of the temperature increase after each neutron pulse is given by

$$\Delta T = 2q_o/(nc\rho r) \quad . \qquad \text{(III.7)}$$

In arriving at this estimate it was tacitly assumed that no heat transfer to the coolant takes place during the duration of the neutron pulse, τ_o. It will be seen in the next section that this assumption is well justified.

With the materials parameters listed in Table III.1, the temperature increase ΔT can be obtained. As seen from Table III.1, the values for ΔT are quite small, i.e., only a few degrees. Consequently, the maximum stress amplitude of the thermoelastic wave is of the order of 10 MPa or below, as seen from the values listed in the last row of Table III.1. Since these values are at least an order of magnitude lower than the fracture strength (for which typical values are also found in Table III.1), the fuel pellets will not disintegrate or even fracture by virtue of the pulsed neutron irradiation. It should be noted that this conclusion is independent of the neutron pulse duration τ_o as long as $\tau_o < \tau_1 \cong 2\mu s$.

IV. Thermal Cycling

Because of the small temperature rise in the fuel during one neutron pulse, effects of thermal cycling such as fuel cracking and fatigue of the cladding are certainly of little concern for the SOLASE-H enrichment procedure.

On the other hand, various alternative fusion hybrid designs with an inertial fusion driver have been studied, in which substantial neutron moderation has been obtained. One of the reasons to moderate the neutrons was to achieve a sufficiently gradual heating rate $\Delta T/\tau_0$ in the fuel in order to avoid a thermal shock. However, this approach to the problem seems to be self-defeating for two reasons.

First, in order to avoid the thermal shock by rapid heating, the neutron pulse duration τ_0 must be substantially larger than τ_1. Suppose that we want to obtain a pulse duration of $\tau_0 = 10\tau_1 \cong 20$ μs which would reduce the maximum stress amplitude by a factor of ten according to the lower part of Eq. (III.3).

From Table IV.1 we find that almost any moderator will slow down the fusion neutrons to very low, if not thermal, energy. Hence, the fission rate in the blanket goes up, increasing ΔT even further.

Second, even if a strong thermal shock could be avoided, large temperature fluctuations become of great concern, as the fuel temperature decreases between successive neutron pulses.

We may characterize the temperature decay rate by the thermal response time

$$\tau_2 = \rho c r^2/\lambda\ \mu_1^2 \qquad \text{(IV.1)}$$

valid for a cylindrical fuel element. Here, λ is the thermal conductivity, and μ_1 the first root of the zero-order Bessel function which has the

Table IV.1

Moderation Parameters for
14 MeV Neutrons

Moderator	Neutron Energy (eV) after 20 μs	Thermalization time (μs)
Water	0.025	11
Heavy Water	0.16	50
Lithium	0.44	90
Graphite	1.4	160
Sodium	5.6	300

value of $\mu_1 = 2.405$. Computed values for τ_2 are given in Table IV.2 for three types of fuel. It is seen that metal and carbide fuel have thermal decay times of the order of one second because of their good thermal conductivity. Thermal cycling is therefore extremely severe for a repetition rate of 4 fusion pellet burns per second. On the other hand, oxide fuel has a thermal decay time of several seconds, and thermal cycling would be somewhat less severe. Nevertheless, even in this case, the fuel temperature at the cladding interface would decrease sufficiently to cause cracking of the outer pellet layer. The continuous thermal cycling and ratcheting could then push small pieces of fuel into the cladding which would cause fuel element failure and fission gas release.

Based on the present assessment we must conclude that neutron moderation is not a feasible approach to avoid the thermal shock problem in a laser fusion hybrid enrichment facility. Rather, neutron moderation must be avoided, as done in SOLASE-H, and the thermal shock problem never arises.

Table IV.2

Fuel	U	Th	UC	ThO_2	UO_2
Thermal Conductivity λ[W/m/°K]	32.2	45.2	23.0	3.2	2.1
Thermal Response Time τ_2[s]	1.5	0.5	0.9	4.7	8.0

V. Fuel Pin and Fuel Assembly Bowing

V.1. Bowing in Light Water Reactors

Bowing of fuel pins and of entire fuel assemblies is a commonly observed phenomenon in LWRs as well as in LMFBRs.

Fig. V.1 shows an example from the Duke Power Company Oconee-1 reactor. The magnitude and direction of the bow for five assemblies is indicated after two consecutive cycles for five assemblies which were moved to a new location after the first cycle without rotation. It is seen that the bow after both cycles is generally outward away from the core center.

The bow of individual fuel pin rods at the midspan between spacer grids is shown in Fig. V. 2 as a function of the assembly burnup.[3] Unequal bow of adjacent fuel pins may result in a change of the rod to rod gap, thereby affecting the fluid flow and heat transfer to the coolant. Therefore, excessive fuel pin bowing must be avoided.

The bow of entire fuel assemblies may result in interactions between adjacent assemblies, so that large frictional forces must be overcome when one assembly is being extracted in the shuffling procedure. This could result in failure and damage to an assembly. Again, it is therefore important to avoid the excessive bow of fuel assemblies.

Whereas the bow of fuel assemblies and of fuel pins in LWRs appears to be primarily due to a relaxation of thermal stresses while the reactor is on power, bowing in a fast neutron flux can also be produced by differential swelling of the fuel element cladding when exposed to flux and temperature gradients. Such a situation arises for example in the SOLASE-H laser fusion hybrid reactor within the fuel breeding zone. Accordingly, a detailed analysis of this bowing problem is given in the following.

FUEL ASSEMBLY BOW AT OCONEE-1

EOC-1 TO EOC-2

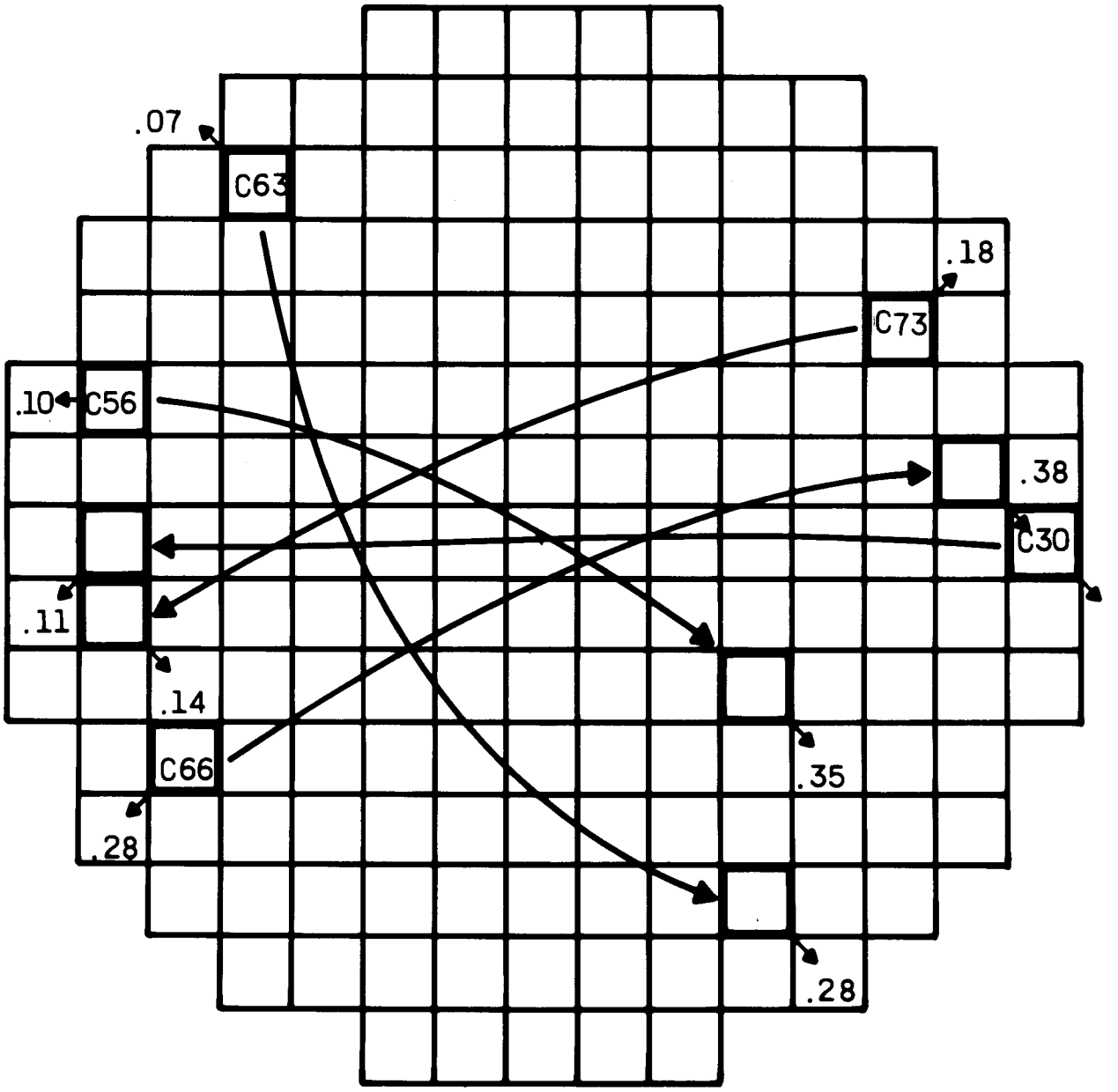

CYCLE 2 LOCATION

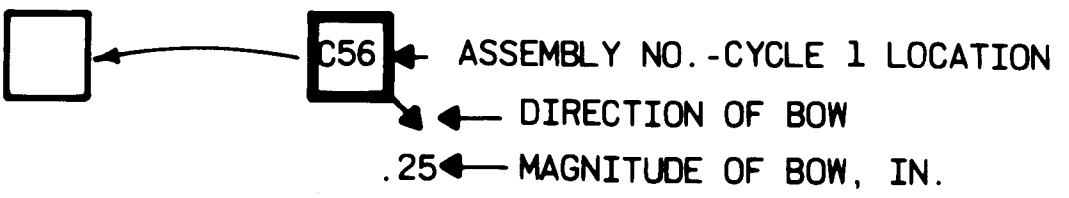

Fig. V.1

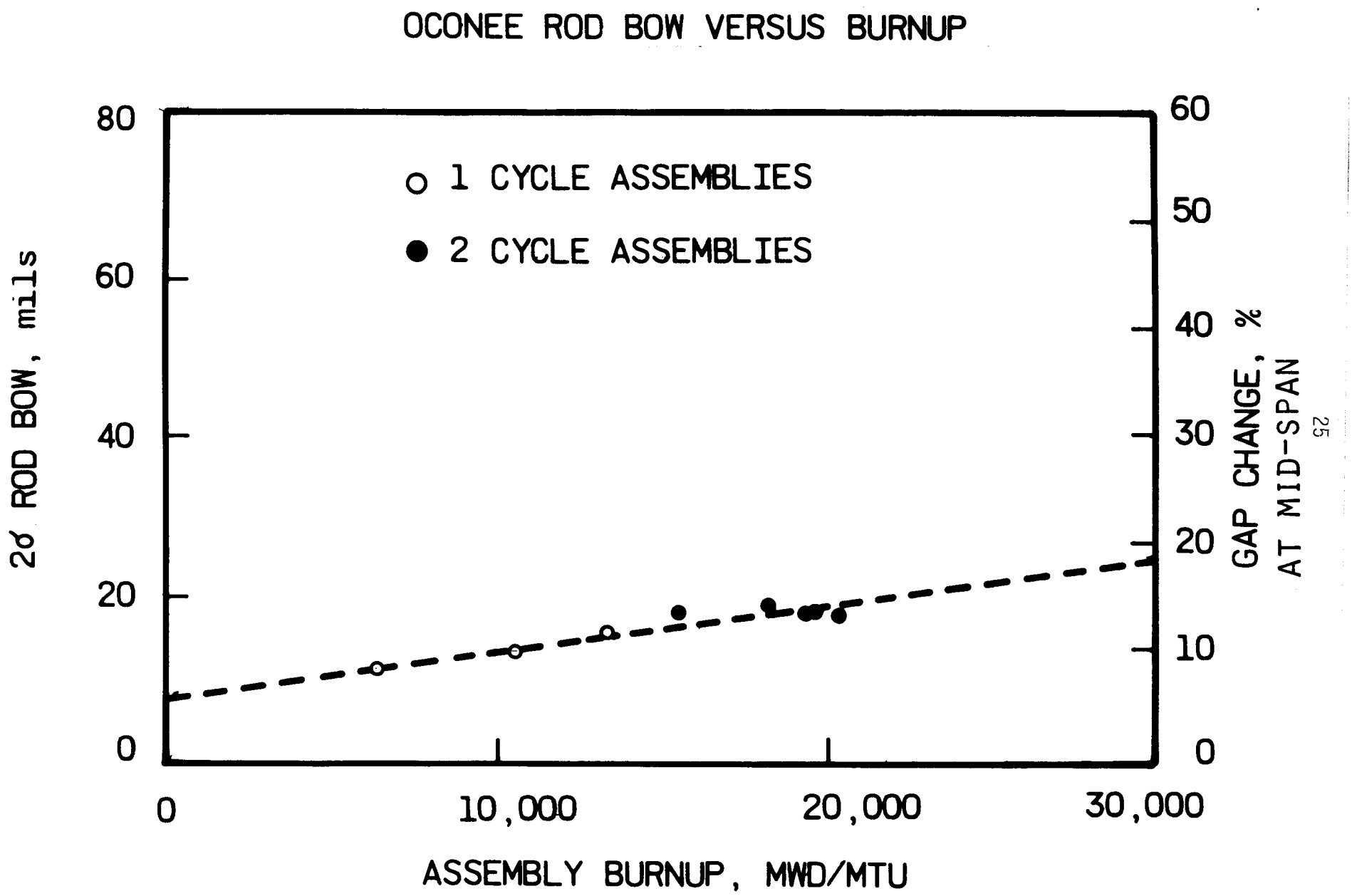
OCONEE ROD BOW VERSUS BURNUP
1 CYCLE ASSEMBLIES
2 CYCLE ASSEMBLIES
2σ ROD BOW, mils
GAP CHANGE, % AT MID-SPAN
ASSEMBLY BURNUP, MWD/MTU
0
20
40
60
80
0
10
20
30
40
50
60
0
10,000
20,000
30,000

Fig. V.2.

V.2. Derivation of the Equation for Fuel Pin Bowing

In a cylindrical coordinate system, as shown in Fig. V.3, the time derivative of Hooke's law can be written as

$$\dot{\sigma}_\theta/2G = \dot{\varepsilon}_\theta - \dot{e}_\theta + \frac{\nu}{1-2\nu}\ (\dot{\varepsilon} - \dot{e}) \tag{V.1}$$

$$\dot{\sigma}_r/2G = \dot{\varepsilon}_r - \dot{e}_r + \frac{\nu}{1-2\nu}\ (\dot{\varepsilon} - \dot{e}) \tag{V.2}$$

$$\dot{\sigma}_z/2G = \dot{\varepsilon}_z - \dot{e}_z + \frac{\nu}{1-2\nu}\ (\dot{\varepsilon} - \dot{e}) \tag{V.3}$$

where σ_θ, σ_z, and σ_r are the hoop, the axial, and the radial stress, respectively, G is the shear modulus and ν the Poisson's ratio. The total strain components are denoted by ε_θ, ε_z, and ε_r, whereas the inelastic strain components are e_θ, e_z, and e_r. The sum of the total strain components is ε, and e is the sum of the inelastic strains.

For a thin-walled tube

$$\sigma_r = -\frac{1}{2}\,p \tag{V.4}$$

$$\sigma_\theta = pR/h\ , \tag{V.5}$$

where p is the difference between inside and outside pressure on the cladding, 2R is the tube diameter, and h is the cladding thickness. Upon using the expressions for the stress rates $\dot{\sigma}_r$ and $\dot{\sigma}_\theta$ in Eqs. (V.1) and (V.2), we can solve the resulting equations for $(\dot{\varepsilon}_\theta - \dot{e}_\theta)$ and $(\dot{\varepsilon}_r - \dot{e}_r)$, and insert the result in Eq. (V.1). We then obtain

$$\dot{\sigma}_z/2G = (1+\nu)(\dot{\varepsilon}_z - \dot{e}_z) + [2\nu R/h - 1 - \nu]\dot{p}/4G \tag{V.6}$$

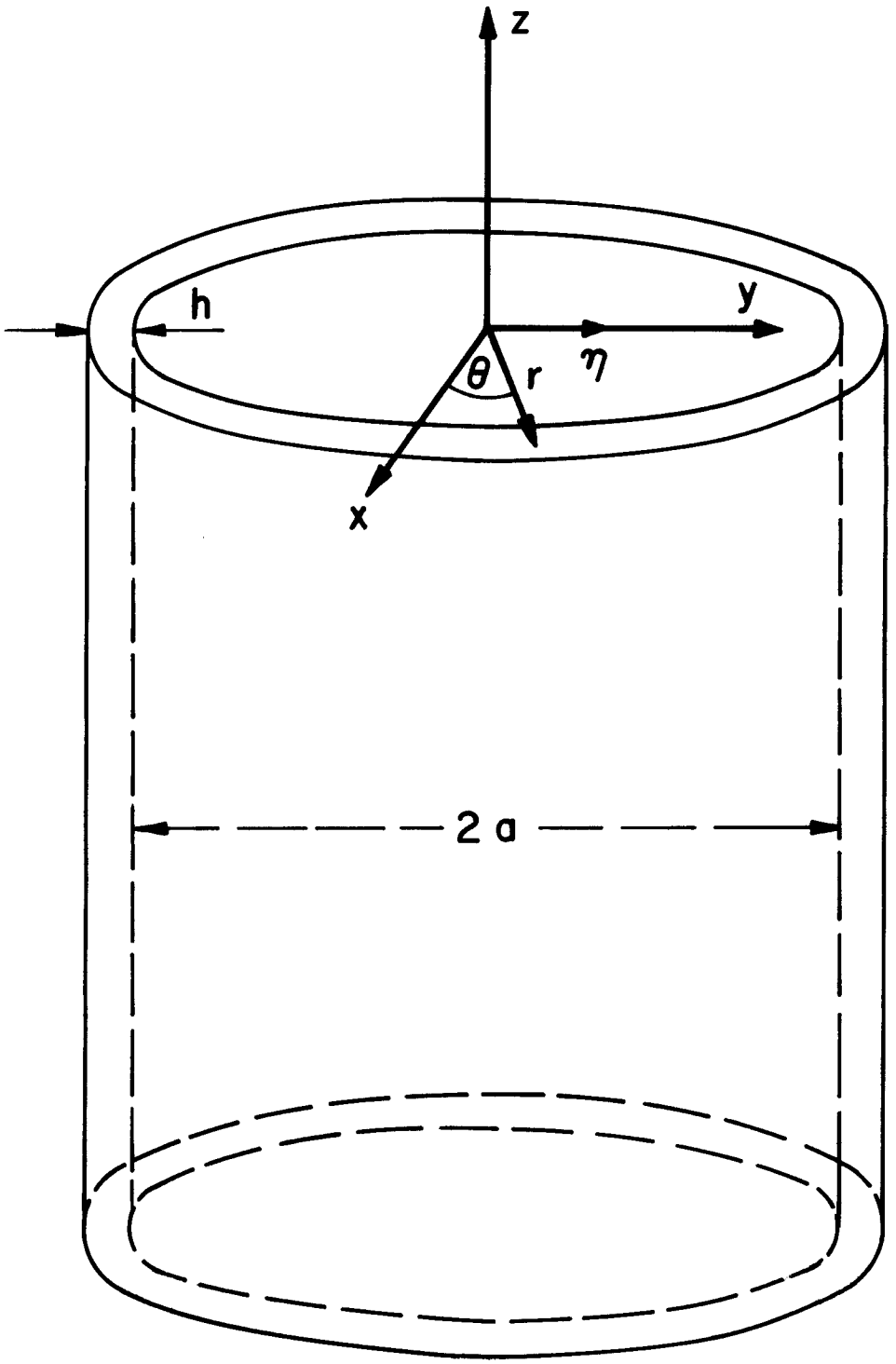

Fig. V.3. Section of Fuel Element Cladding.

If the tube bends in the (y,z) plane, the axial strain component is given by

$$\varepsilon_z = \langle\varepsilon_z\rangle - \eta \frac{d^2w}{dz^2} \quad , \tag{V.7}$$

where $\langle\varepsilon_z\rangle$ is the axial strain averaged over the cross-section, w(z) the lateral deflection of the axis from its straight line, i.e., the location of the centroidal axis, and η is the distance from this centroidal axis.

If no axial forces act on the fuel pin other than the internal gas pressure and the external fluid pressure, the average of the axial stress is given by

$$\langle\sigma_z\rangle = \frac{1}{A}\int dA\sigma_2 = \frac{Rp}{2h} \quad , \tag{V.8}$$

where A is the cross-section area of the cladding. Hence, if we take the average of Eq. (V.6) we obtain

$$\langle\dot{\varepsilon}_z\rangle = \langle\dot{e}_z\rangle + \left[\frac{1-2\nu}{1-\nu}\frac{R}{h} + 1\right]\frac{\dot{p}}{4G} \quad . \tag{V.9}$$

Inserting this result into Eq. (V.7) and subsequently into Eq. (V.6), we may write

$$\dot{\sigma}_z/E = -\eta \frac{d^2\dot{w}}{dz^2} + \langle\dot{e}_z\rangle - \dot{e}_z + \frac{R\dot{p}}{2hE} \quad , \tag{V.10}$$

where $E = 2G(1+\nu)$ is the Young's modulus.

The inelastic deformation rate is caused by swelling and irradiation creep. For the axial direction

$$\dot{e}_z = \frac{1}{3}\dot{S} + \psi\left(\sigma_z - \frac{1}{2}\sigma_\theta - \frac{1}{2}\sigma_r\right) \cong \frac{1}{3}\dot{S} + \psi\left(\sigma_z - \frac{Rp}{2h}\right) \qquad (V.11)$$

where we used Eq. (V.5) for σ_θ and neglected σ_r.

The swelling rate $\dot{S}$ as well as the creep compliance ψ change across the fuel pin because of the flux and temperature gradients. We may write

$$\dot{S} \cong \langle\dot{S}\rangle + \nabla\dot{S}\,\eta \qquad (V.12)$$

$$\psi = \langle\psi\rangle + \nabla\psi\,\eta\ , \qquad (V.13)$$

where $\nabla\dot{S}$ is the swelling rate gradient and $\nabla\psi$ the creep compliance gradient.

With these expressions we obtain

$$\langle\dot{e}_z\rangle = \frac{1}{3}\langle\dot{S}\rangle + \langle\psi\rangle\left\langle\left(\sigma_z - \frac{Rp}{2h}\right)\right\rangle + \nabla\psi\,\frac{1}{A}\int dA\,\eta\sigma_z \quad .$$

Since $\langle\sigma_z\rangle = Rp/2h$, the second term vanishes. Using the definition

$$M = \int dA\ \eta\sigma_z$$

for the bending moment, we find

$$\langle\dot{e}_z\rangle = \frac{1}{3}\langle\dot{S}\rangle + \nabla\psi\cdot M/A \qquad (V.14)$$

and

$$\dot{\sigma}_z/E = -\eta\,\frac{d^2\dot{w}}{dz^2} + \frac{1}{3}\left(\langle\dot{S}\rangle - \dot{S}\right) + \nabla\psi M/A - \psi\left(\sigma_z - \frac{Rp}{2h}\right) + \frac{R\dot{p}}{2hE} \quad . \qquad (V.15)$$

If this equation is multiplied by (η/A), then integrated over the cross-section of the cladding, one obtains finally

$$\boxed{\frac{d^2\dot{w}}{dz^2} + \frac{1}{EI}\dot{M} + \frac{\langle\psi\rangle}{I}\,M = -\frac{1}{3}\nabla\dot{S}} \qquad (V.16)$$

where the moment of inertia around the x-axis is defined as

$$I = \int \eta^2 dA \cong \pi R^3 h \qquad (V.17)$$

for a single fuel element.

The Eq. (V.16) may also be applied to the bowing of the entire fuel assembly. In this case, the frame consisting of the spacer grids attached rigidly to the control-rod guide tubes constitutes a "beam" with a moment of inertia given by

$$I_A = N_{cr} I + 2\pi R h \sum_i x_i^2 \qquad (V.18)$$

where N_{cr} is the number of control rod guide tubes and x_i their distance from the neutral plane.

For LWR fuel pins, $I = 0.016$ cm^4, and assuming that there are 24 control rods for one assembly, $I_A \cong 100$ cm^4.

V.3. Evaluation of the Reaction Forces

The fuel elements in an assembly are held in their vertical position by the spacer grids. In turn the lateral motion of these grids is restrained by adjacent assemblies in the LWR core. In the hybrid reactor, the lateral motion of the grids is prevented by a shroud forming an integral part of the blanket structure.

Both the bowing of individual fuel pins as well as the entire fuel assembly is therefore restrained at certain axial positions L_j where the spacer grids are located. Fig. V.4 shows a schematic of this bowing model. The reaction forces between the fuel pin and the grids, or between the grids and the shroud, are denoted by F_j.

Excessive bowing may produce significant reaction forces so that the extraction of the fuel assembly from the blanket region may be difficult. It is therefore necessary to evaluate these reaction forces.

At the axial location z, the bending moment is given by

$$M(z) = \sum_{j=0}^{N} \theta(z-L_j)(z-L_j)F_j \qquad (V.19)$$

where $L_o = 0$ and

$$\theta(z-L_j) = \begin{cases} 0 & \text{if } z < L_j \\ 1 & \text{if } z \geq L_j \end{cases} . \qquad (V.20)$$

The (N+1) reaction forces must satisfy the following balance equations

$$\sum_{j=0}^{N} F_j = 0 \qquad (V.21)$$

and

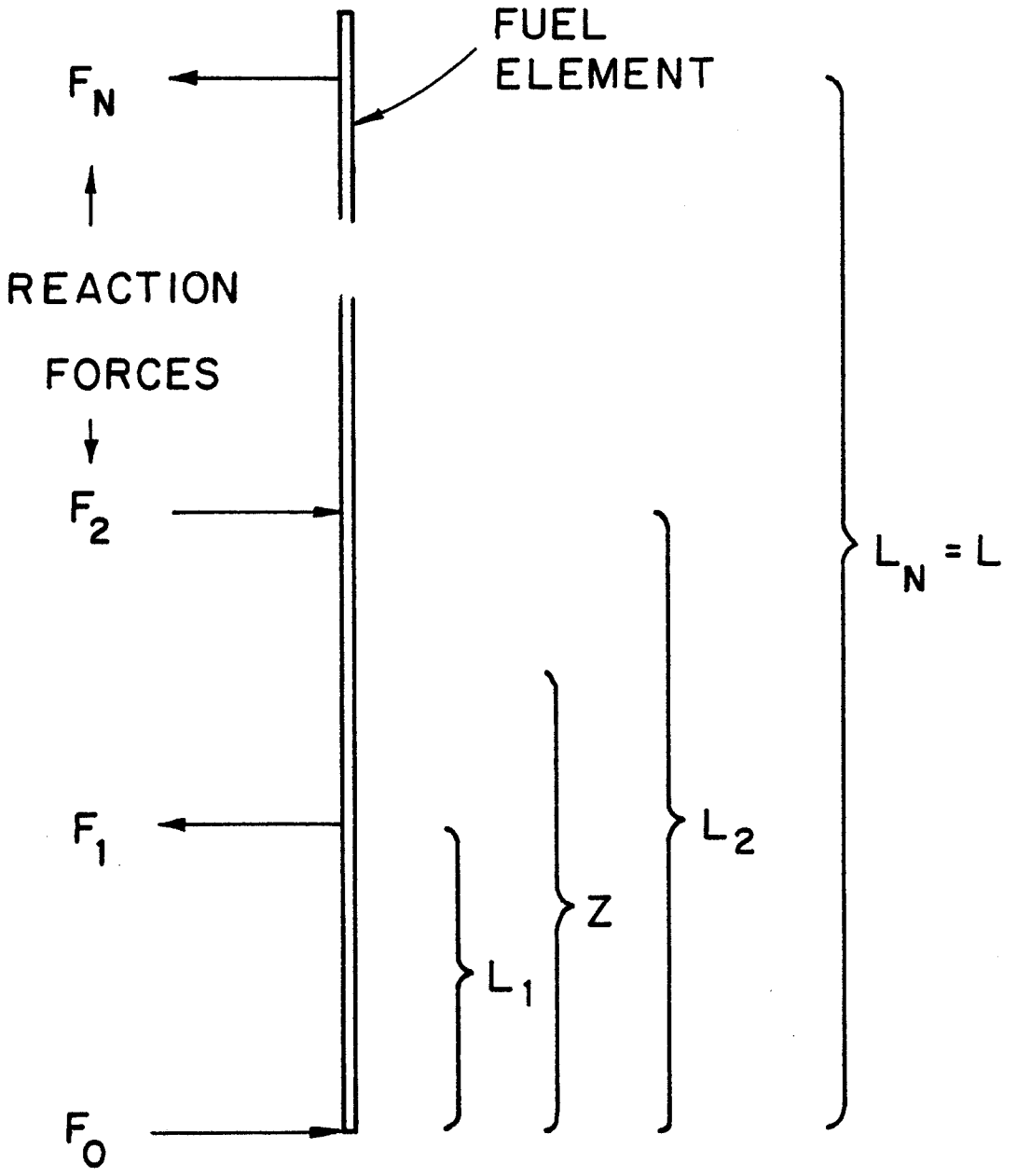

Fig. V.4. Bowing Model of a Fuel Element with Reaction Forces F_i Generated by the Grid Spacers.

$$\sum_{j=0}^{N} L_j F_j = 0 \quad . \tag{V.22}$$

Eq. (V.19) is now inserted into Eq. (V.16) and the latter integrated twice. We obtain

$$-\dot{w}(z) = C_1 + C_2 z + \dot{\zeta}(z) + \frac{1}{6EI} \sum_{j=0}^{N} \dot{F}_j \, \theta(z-L_j)(z-L_j)^3 + \frac{1}{I} \sum_{j=0}^{N} F_j \, \theta(z-L_j) \, \xi_j(z) \quad , \tag{V.23}$$

where

$$\dot{\zeta}(z) = \frac{1}{3} \int_0^z dx \int_0^x dy \, \nabla \dot{S}(y) \tag{V.24}$$

and

$$\xi_j(z) = \int_{L_j}^{z} dx \int_{L_j}^{x} dy (y-L_j) \langle \psi(y) \rangle \tag{V.25}$$

The integration constants C_1 and C_2 as well as the reaction forces are determined by the conditions

$$\dot{w}(L_i) = 0 \quad \text{for } i = 0,1,\ldots,N \tag{V.26}$$

and by the Eqs. (V.21) and (V.22).

For equidistant spacing of the grids

$$L_j = (j-1) \, \Delta L \quad , \quad j=1,\ldots,N \tag{V.27}$$

and the above conditions lead to the following system of equations:

$$\sum_{j=0}^{i-1} \left[\frac{\Delta L}{6E} (i-j)^3 \dot{F}_j + \xi_{ij} F_j \right] = - \, iC - \dot{\zeta}_i \quad , \tag{V.28}$$

where

$$C = IC_2/\Delta L$$

$$\dot{\zeta}_i = \frac{1}{3}\frac{I}{(\Delta L)^2}\int_0^{L_i} dx \int_0^x dy\, \nabla\dot{S}(y) \qquad (V.29)$$

and

$$\xi_{ij} = \frac{I}{(\Delta L)^2}\int_{L_j}^{L_i} dx \int_{L_j}^x dy(y-L_j)\langle\psi(y)\rangle \quad . \qquad (V.30)$$

The system of differential equations (V.28) has an asymptotic steady-state solution $\dot{F}_i = 0$ if the differential swelling rate $\nabla\dot{S}$ reaches a constant value. This is indeed the case at doses above the incubation period, whereas below this period, $\nabla\dot{S} \simeq 0$.

The steady-state solution of Eq. (V.28) can be written as

$$F_{i-1} = -(CA_i + B_i)/D \quad , \qquad (V.31)$$

where D is the determinant of the matrix

$$\begin{pmatrix} \xi_{10} & 0 & 0 & \cdots & 0 \\ \xi_{20} & \xi_{21} & 0 & \cdots & 0 \\ \cdots & \cdots & \cdots & \cdots & \cdots \\ \xi_{N0} & \xi_{N1} & \xi_{N2} & \cdots & \xi_{N,N-1} \end{pmatrix} \quad , \qquad (V.32)$$

A_i is the determinant of a matrix obtained from (V.32) by replacing the i-th column with the column vector

$$\begin{pmatrix} 1 \\ 2 \\ \cdot \\ \cdot \\ \cdot \\ \cdot \\ \cdot \\ N \end{pmatrix} \quad ,$$

and B_i is the determinant of a matrix obtained from (V.32) when the vector

$$\begin{pmatrix} \dot{\zeta}_1 \\ \dot{\zeta}_2 \\ \cdot \\ \cdot \\ \cdot \\ \cdot \\ \dot{\zeta}_N \end{pmatrix}$$

replaces the i-th column.

The constant C is determined from Eq. (V.22), written in the form

$$\sum_{i=0}^{N-1} iF_i + NF_N = 0 \quad .$$

Upon inserting the solution (V.31), we obtain

$$C = - \sum_{i=0}^{N-1} (N-i)B_i / [\sum_{i=0}^{N-1} (N-i)A_i] \quad . \tag{V.33}$$

For the numerical evaluation, the integrations in Eqs. (V.29) and (V.30) must be carried out over the axial variation of both the swelling rate and the irradiation creep rate. A simple, but sufficiently accurate estimate may be obtained by using average values $\nabla\dot{S}_{av}$ and ψ_{av} for these quantities. Then

$$\dot{\zeta}_i = \frac{1}{6} I \, i^2 \, \nabla\dot{S}_{av} \tag{V.34}$$

$$\dot{\xi}_{ij} = \frac{1}{6} I \, \psi_{av} \, \Delta L \, (i-j)^3 \tag{V.35}$$

and the determinants A_i and B_i are given by

$$A_i/D = (-1)^{i-1}\, d_i^{(13)}\, \frac{6}{I\Delta L\psi_{av}} \tag{V.36}$$

$$B_i/D = (-1)^{i-1}\, d_i^{(23)}\, \frac{\nabla \dot{S}_{av}}{\Delta L\psi_{av}} \tag{V.37}$$

where the determinants $d_i^{(n3)}$ are defined as

$$d_i^{(n3)} = \begin{vmatrix} 1^n & 1^3 & 0 & \cdots & 0 \\ 2^n & 2^3 & 1^3 & \cdots & 0 \\ 3^n & 3^3 & 2^3 & \cdots & 0 \\ \cdot & \cdot & \cdot & \cdots & \cdot \\ \cdot & \cdot & \cdot & \cdots & \cdot \\ \cdot & \cdot & \cdot & \cdots & \cdot \\ \cdot & \cdot & \cdot & \cdots & 1^3 \\ i^n & i^3 & (i-1)^3 & \cdots & 2^3 \end{vmatrix}$$

Their numerical values are listed in Table V.1.

Table V.1

i	$d_i^{(13)}$	$d_i^{(23)}$
1	1	1
2	6	4
3	24	14
4	90	52
5	336	194
6	1254	724
7	4680	2702
8	17466	10084
9	65184	37634
10	243270	140452

A typical LWR fuel assembly has seven spacer grids. Hence with N=7 we find from Eqs. (V.31) and (V.33) the following reaction forces listed in Table V.2.

Table V.2

Reaction Forces

i	$F_i/[\frac{I}{\Delta L}\frac{\nabla\dot{S}_{av}}{\psi_{av}}]$
0	+0.4225
1	-0.5325
2	+0.1409
3	-0.0282
4	-0.0282
5	+0.1409
6	-0.5325
7	+0.4225

The pull force to extract a fuel pin is proportional to the absolute values of all reaction forces. From Table V.2 we find that

$$\sum_{i=0}^{N} |F_i| = 2.2536 \frac{I\nabla\dot{S}_{av}}{\Delta L\ \psi_{av}} \qquad (V.38)$$

The differential swelling rate across the fuel pin or the assembly may be written as

$$\nabla\dot{S}_{av} \cong \frac{d\dot{S}}{dT}\nabla T \qquad (V.39)$$

where $d\dot{S}/dT$ is the temperature derivative of the swelling rate shown in Fig. V.5 for a dose rate of 2×10^{-7} dpa/sec for type 316 stainless steel. ∇T is the temperature gradient across the fuel pin or the fuel assembly.

The irradiation creep compliance ψ_{av} for type 316 stainless steel is shown in Fig. V.6, and the quantity $(d\dot{S}/dT)(1/\psi_{av})$ in Fig. V.7.

Since a detailed thermo-hydraulic analysis of the coolant flow through the blanket region in the SOLASE-H reactor was not performed we use the

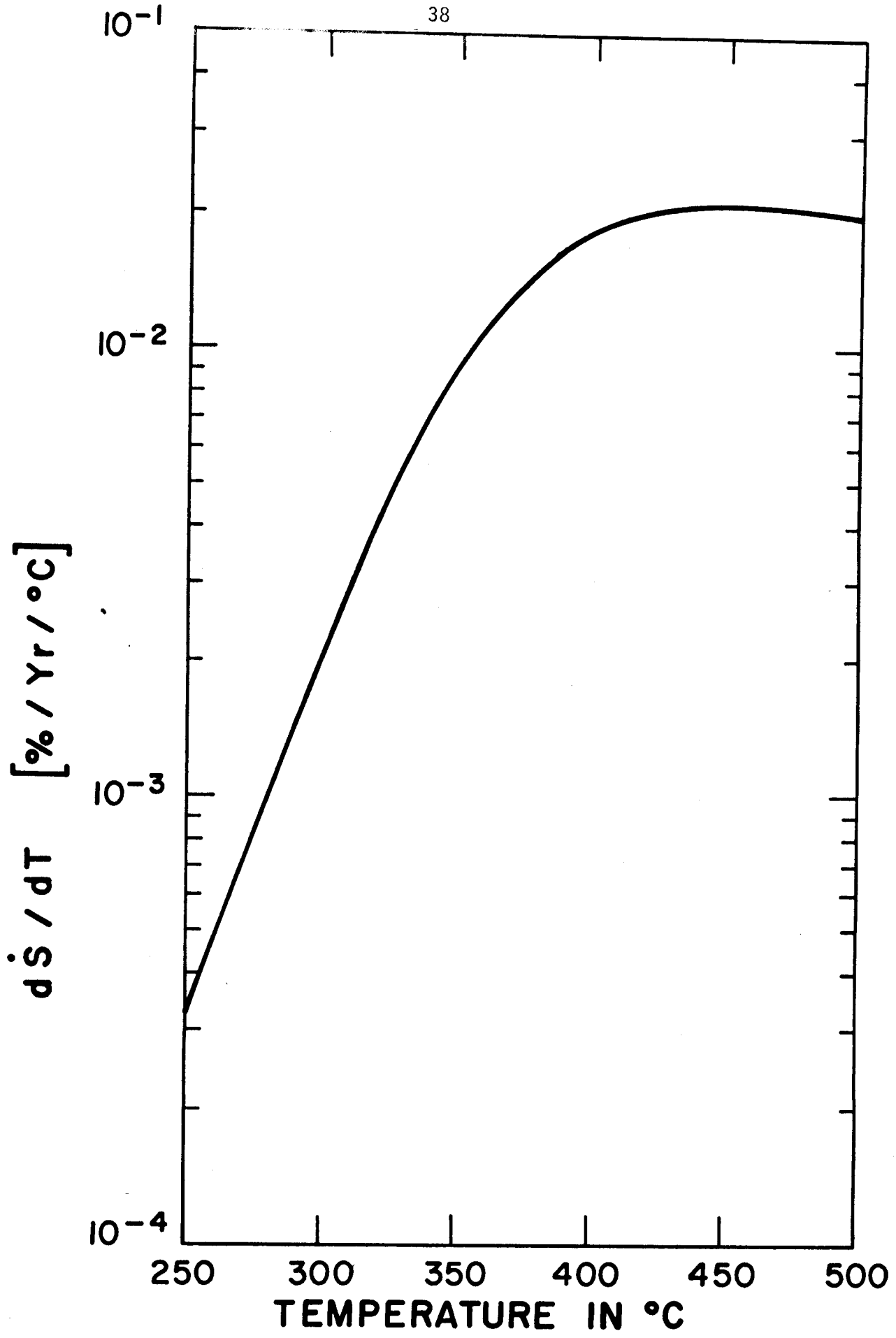

Fig. V.5. Temperature Derivative of the Swelling Rate of Type 316 Stainless Steel.

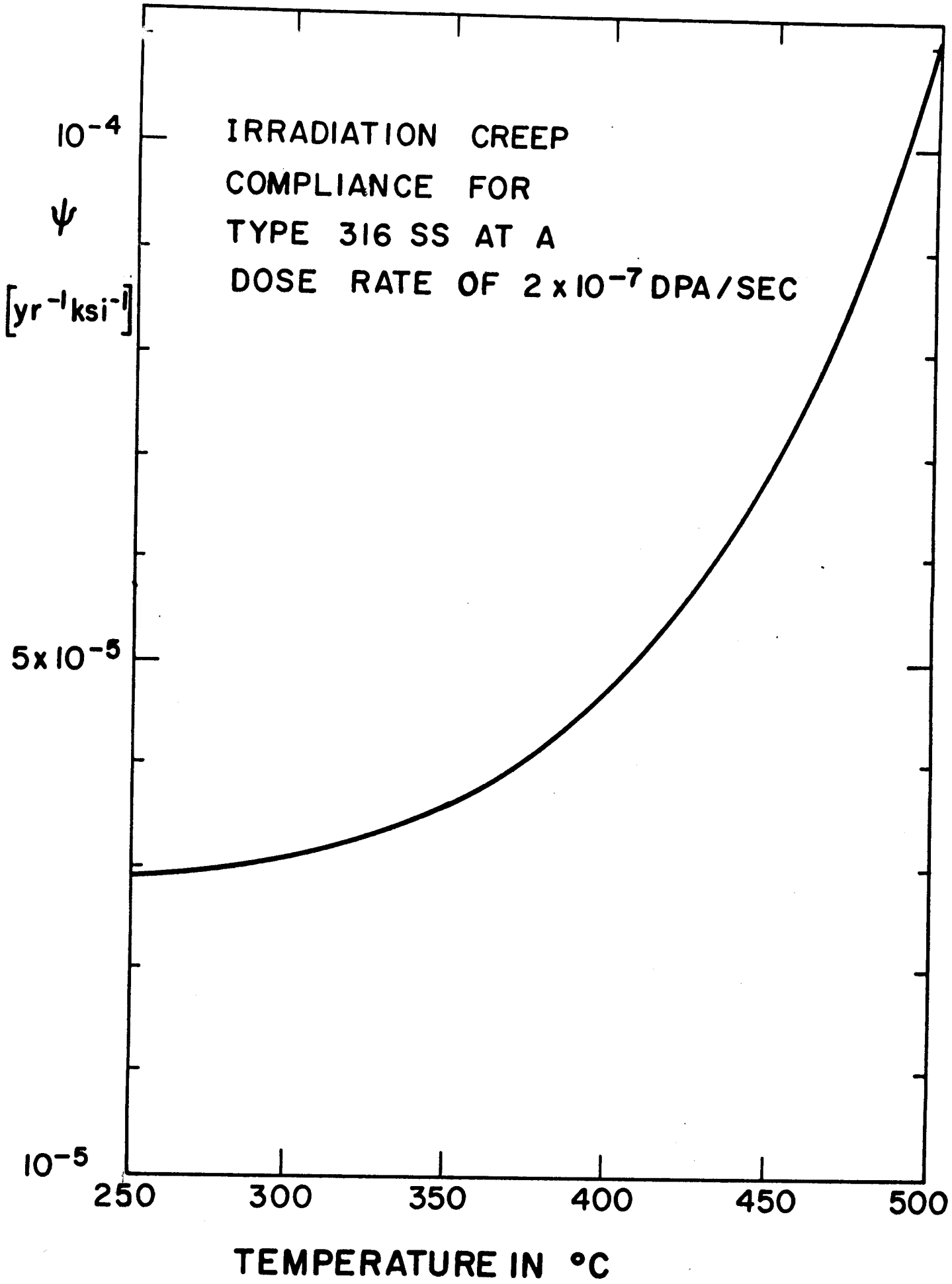

Fig. V.6. Temperature Dependence of the Irradiation Creep Rate for Type 316 Stainless Steel.

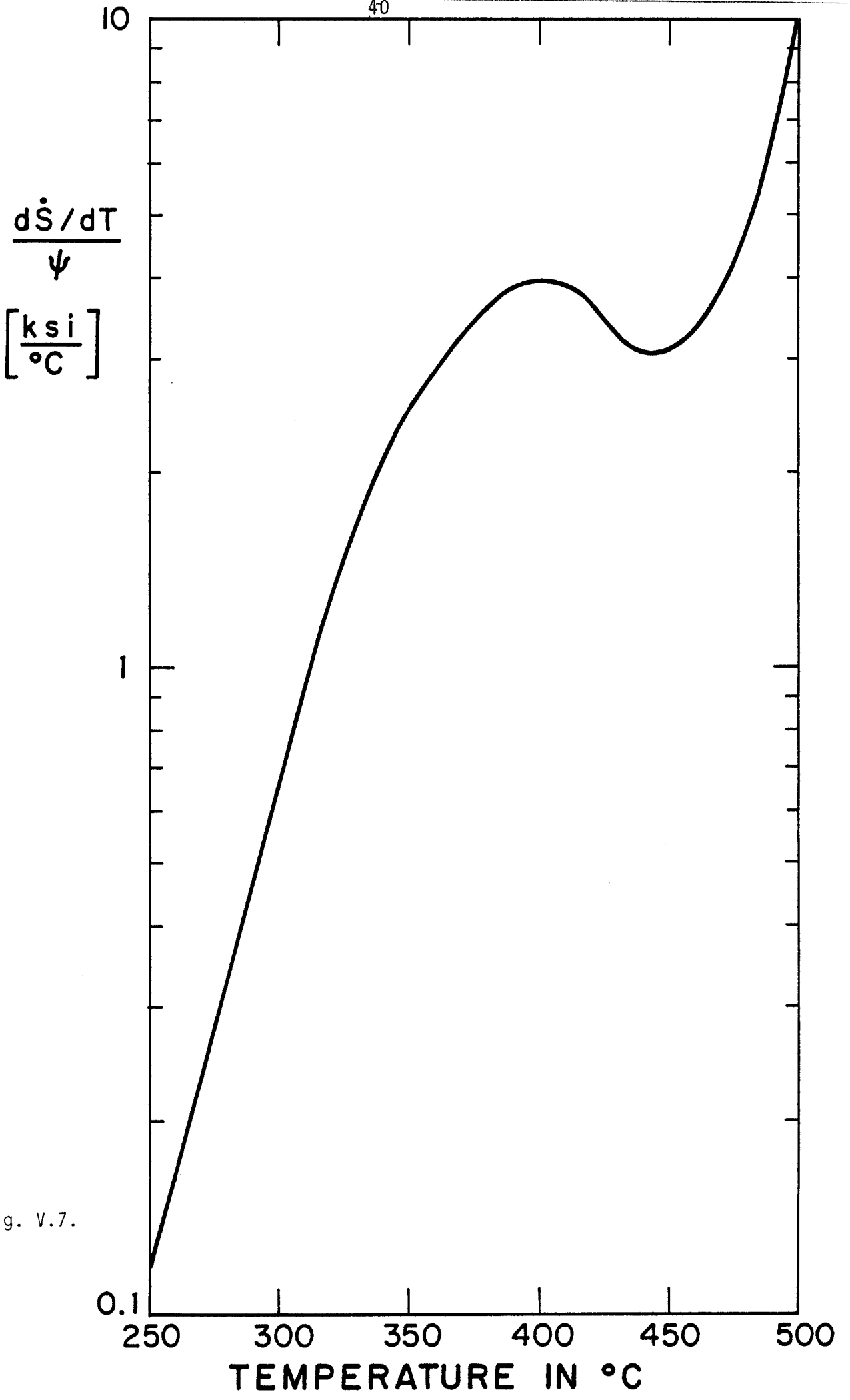
10
1
0.1
$\frac{d\dot{S}/dT}{\psi}$
$\left[\frac{ksi}{°C}\right]$
250
300
350
400
450
500
TEMPERATURE IN °C

Fig. V.7.

following estimates for the temperature gradient across individual fuel pins and across the fuel assembly. The temperature difference on opposite sides of the fuel element cladding is assumed to be 4°C or lower, so that the temperature gradient is $\nabla T \leq 4/0.89 \cong 4.5°/cm$.

Since the outlet coolant temperature is 350°C, the ratio of $d\mathring{S}/dT$ and ψ_{av} is, according to Fig. V.7, not larger than 2.5 ksi/°C. Using this value in Eq. (V.28) and the value of $\Delta L = 0.52$ m, we find that for a fuel pin

$$\sum |F_i| \leq 5.38 \text{ N} \quad .$$

Assuming that the bow of all 289 fuel pins is the same, their total lateral force on all spacer grids is $\leq$1554.6 N. With a friction coefficient of 0.2 between the spacer grids and the shroud, we compute a pull force of

$$B \leq 311 \text{ N} \quad . \tag{V.40}$$

Next, if we apply Eq. (V.39) to the frame of the spacer grids rigidly attached to the control rod guide tubes, we simply replace I by I_A of Eq. (V.18) and obtain a total lateral force of

$$\sum |F_i| \leq 33{,}578 \text{ N}$$

and a pull force of

$$B \leq 6715 \text{ N} \cdot \tag{V.41}$$

This is comparable to the weight of the fuel assembly itself, namely 6900 N. However, it must be noted that the present estimate is very

conservative for two reasons. First, the maximum possible swelling gradient was assumed to exist along the entire fuel assembly. Second, a rigid rather than flexible connection between the spacer grids and the control-rod guide tubes was modeled. For these reasons the pull force is significantly less than the estimate provided by Eq. (V.41), and we conclude that the bowing should not pose a critical problem for the extraction of the enriched fuel assemblies from the SOLASE-H reactor and the insertion into the LWR core.

References for Sections I to V.

1. R. W. Conn et al., SOLASE-H, "A Laser Fusion Hybrid Study," UWFDM-270, University of Wisconsin, May 1979.

2. J. M. Dupouy, "French Program on LMFBR Cladding Materials Development," in Rad. Effects in Breeder Reactor Structural Materials, ed. by M.L. Bleiberg and J.W. Bennett, AIME, 1977.

3. M.H. Montgomery, J.T. Mayer, and D.F. Frechi, "A Review of the B & W Company and Duke Power Company Post Irradiation Examination Program," ANS Topical Meeting on Water Reactor Fuel Performance, 1977, p. 71.

VI. Sodium Compatibility Considerations for Hybrid Reactor Materials

VI.1. Introduction

The investigation of the compatibility of sodium with potential structural materials for the fusion hybrid reactor SOLASE-H was motivated by the design criterion to employ sodium instead of lithium as coolant in order to minimize the tritium inventory. This study focuses on two specific areas:

1. Sodium-Zircaloy compatibility,
2. Sodium removal from LWR fuel subassemblies.

These topics are of particular interest primarily because of the proposal to design the hybrid reactor such that when Zircaloy clad LWR fuel subassemblies are sufficiently depleted in the fissile isotope U-235, they could be removed from the LWR and inserted into the sodium cooled blanket region of the hybrid reactor where the high energy fusion neutrons would transmute the remaining large quantities of U-238 into fissile Pu-239. In this regard, the fusion hybrid would effectively act as an enrichment facility. Once the desired plutonium enrichment is attained, the fuel subassemblies could be removed from the liquid sodium environment, cleaned of the sodium, inspected, and then reinserted back into the water environment of the LWR. This scenario establishes the need for an investigation into both the compatibility of sodium with Zircaloy as well as possible techniques of sodium removal from fuel subassemblies. In addition, the proposal to use Zircaloy as a first wall material as well as for other structural components within the reactor reinforces the need to investigate sodium-Zircaloy compatibility.

VI.2. Sodium-Zircaloy Compatibility

The dominant corrosion process in a liquid sodium-Zircaloy system consists of the oxidation of zirconium due to dissolved oxygen in the sodium.[1] This process proceeds according to the reaction:

$$Zr + 2Na_2O \rightarrow ZrO_2 + 4Na \quad .$$

Zircaloy-II and Zircaloy-IV contain approximately 98% zirconium as indicated in Table VI.1.[2] The corrosion of Zircaloy consists of a three

Table VI.1: Composition of Zircaloy-II and Zircaloy-IV (weight percent)

	Zr	Be	Fe	Cr	Ni
Zircaloy-II	98%	1.2 - 1.7	0.07 - 0.20	0.05 - 0.15	0.03 - 0.08
Zircaloy-IV	98%	1.2 - 1.7	0.12 - 0.18	0.05 - 0.15	0.007 Max

step process.[3] Initially, a very small amount of zirconium dissolves in the sodium. The saturation concentraction of zirconium in liquid sodium at 350°C is only 0.00002 ppm as computed from the following expression.[4]

$$\ell n\ [Zr]_{SAT} = 5.33 - \frac{5590}{T}$$

Here the saturation concentration of zirconium is in ppm and the temperature T is in degrees celsius. Almost simultaneously with this dissolution, an adherent oxide layer quickly forms on the surface and inhibits further dissolution. Lastly, the oxide layer diffuses into the metal surface at a rate which depends on the oxygen concentration and temperature of the sodium. Essentially, the corrosion problem consists of the growth of this oxide layer.

The oxide layer is advantageous because it inhibits surface diffusion of impurities into the metal such as hydrogen which can cause embrittlement. Consequently, this property may also be valuable in mitigating tritium diffusion. On the other hand, the oxide layer is deleterious because it results in a substantial reduction in fatigue life. This occurs because the oxide surface layer, being harder and more brittle than the substrate metal, acts as a crack initiator. This effect may be of particular concern for a Zircaloy first wall that would experience cyclic thermal stresses caused by pellet microexplosions. Unfortunately, due to limited experimental data, this effect is difficult to quantify.[5]

In regard to reaction kinetics, it has been found that for dissolved oxygen concentrations less than 20 ppm, the oxidation rate is found to decrease with decreasing oxygen concentration and decreasing temperature. Negligible corrosion has been reported for oxygen concentrations less than 5 ppm. On the other hand, for oxygen concentrations greater than 20 ppm and up to 200 ppm, the oxidation rate is independent of oxygen concentration, increasing only with increasing temperature.[6]

For Zircaloy in the absence of irradiation and in both static and dynamic liquid sodium with oxygen concentrations in excess of 20 ppm, experiments indicate that the weight gain (Δw) is given by:

$$\Delta w = (kt)^{1/2}$$

where k is a constant at a given temperature and t is the exposure time in liquid sodium. The value of k can be determined from the graph in Figure VI.1.[4] Table VI.2 indicates exemplary weight gains calculated from

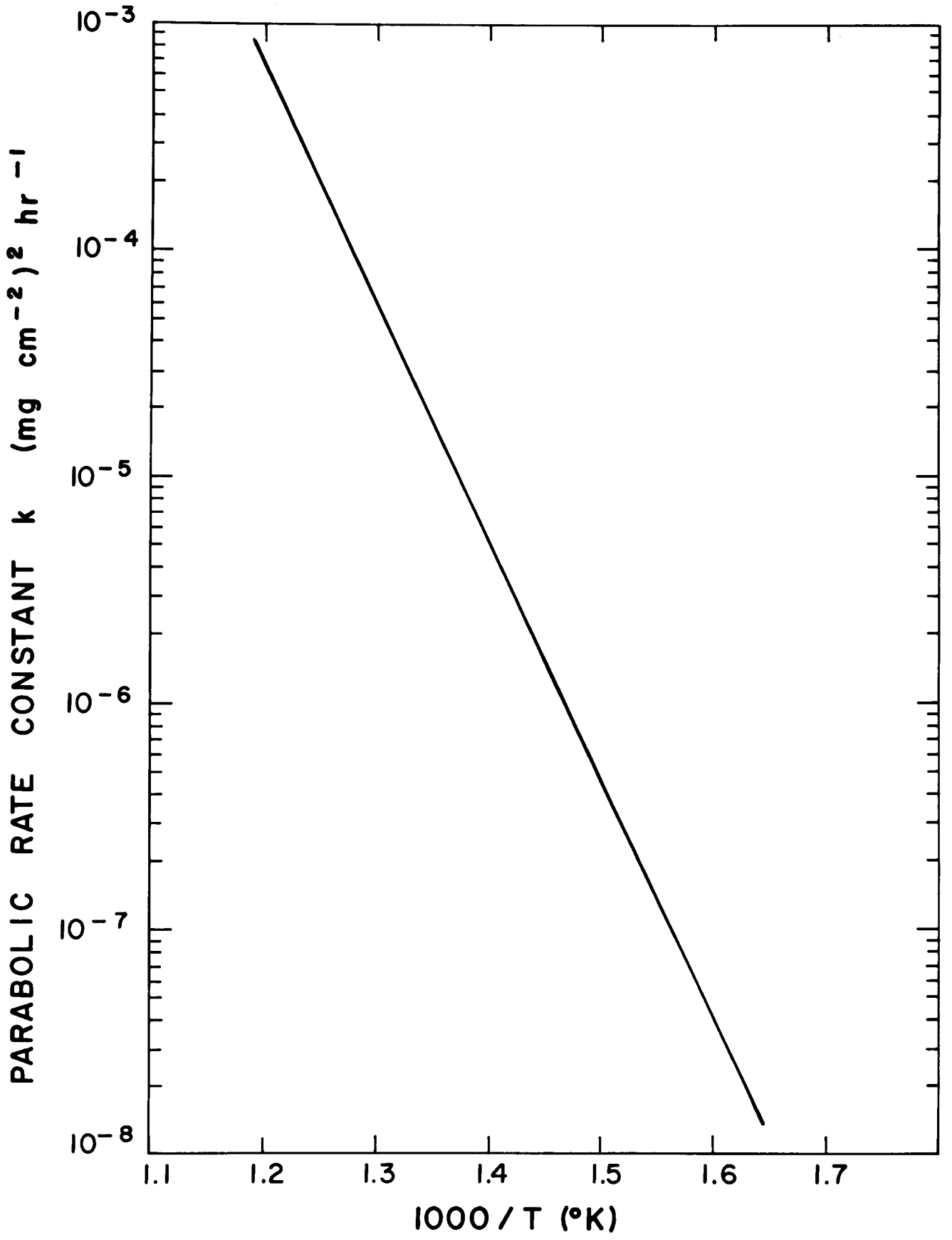

Figure VI.1: Parabolic rate constant for Zircaloy-II in liquid sodium.

this information. It is noteworthy that in light water reactors, high fast neutron flux levels have produced weight gain acceleration by as much as a factor of ten.

Table VI.2: Weight Gain of Zircaloy in Liquid Sodium

Temperature (°C)	k $[(mg\ cm^{-2})^2 hr^{-1}]$	Exposure Time (Years)	Weight Gain (mg/cm^2)	Oxide Thickness* (μm)
350	3.0×10^{-8}	1	0.016	0.109
"	"	2	0.023	0.156
"	"	4	0.032	0.218
400	6.0×10^{-7}	1	0.072	0.490
"	"	2	0.103	0.701
"	"	4	0.145	0.986

*1 μm = 14.7 mg/dm^2

The oxygen concentration in liquid sodium can be effectively controlled to less than 1 ppm by hot trapping a side stream of sodium using either a zirconium or zirconium-titanium alloy getter maintained at approximately 650°C. On the other hand, cold trapping, a process based on the solubility temperature dependence of Na_2O, has a lower limit of 20 ppm for oxygen removal.[6] Consequently, cold trapping alone would prove ineffectual in reducing the corrosion rate since the oxidation rate is independent of oxygen concentration above 20 ppm. But, if it were concluded that the requisite corrosion rate demanded operating in the less than 20 ppm range, a parallel arrangement of hot and cold traps would be useful in deoxygenating severely oxygenated sodium.

In conclusion, the sodium-Zircaloy system proposed for the SOLASE-H fusion hybrid reactor design appears to be, under controlled conditions, a compatible system in regard to corrosion. Essentially, sodium-Zircaloy corrosion consists of the growth of an adherent oxide layer on the metal surface. The growth rate is a function of temperature, oxygen concentration, and most likely irradiation environment. The less oxide the better from the standpoint of extending fatigue life while on the other hand, a certain degree of oxide is beneficial in reducing diffusion of impurities such as the tritium within the fusion hybrid. Negligible corrosion results for oxygen concentrations less than 5 ppm which can be achieved by hot trapping a side stream of sodium.

VI.3. Sodium Removal From LWR Fuel Subassemblies

In order to avoid violent sodium-water reactions and help maintain LWR primary water standards, fuel assemblies removed from the liquid sodium environment of the hybrid reactor must be thoroughly cleaned of sodium before their reinsertion into the water environment of a LWR.

Several of the major factors which will affect the design of such a sodium cleaning system are listed below.

1. Fuel assembly damage,
   a. overheating
   b. thermal shock
   c. thermal stress caused by nonuniform temperature distribution
   d. pressure excursions
   e. corrosion (e.g., stress corrosion cracking)
2. Decay heat removal (maximum permissible fuel clad temperature),
3. Cleaning effectiveness (tolerable residual sodium),
4. Radiation shielding,
5. Radioactive materials containment,
6. Failed fuel detection (sodium logging, bowing, etc.),
7. Waste disposal,
8. Cost, and
9. Simplicity.

In general, all sodium removal procedures that have been used on fuel subassemblies to date consist of four basic steps as follows:

STEP 1: Melt and Drain (m.p. 97.8°C = 208.1°F)

STEP 2: Wash

STEP 3: Water Rinse

STEP 4: Dry

Essentially, these procedures differ only in the process used for the wash step. These processes are of two types, namely reactive cleaning and nonreactive cleaning. Reactive cleaning employs a cleaning agent that reacts chemically with the sodium to form removable reaction products. In this category, water, steam mixed with inert gas, and alcohol have been used successfully. Nonreactive cleaning employs a cleaning agent that dissolves or emulsifies the sodium so that it can be flushed from the subassembly surfaces. Ammonia and oil combined with ultrasonic agitation are two such cleaning agents that have been used with success. In addition, current research into a vacuum distillation process for removing sodium has produced encouraging results. Each of the above mentioned processes will now be discussed in greater detail.

Water has been used as the cleaning agent on fuel subassemblies at the Experimental Breeder Reactor I (EBR-I) and at the Sodium Reactor Experiment (SRE).[7] At EBR-I, the subassemblies were slowly lowered into a water bath in a hot cell, the reaction rate being controlled by regulating the insertion rate. Equivalently, at the SRE, the subassemblies were inserted into a hot cell which was then purged with helium, vented, and then slowly filled with water. The reaction rate control was accomplished by regulating the water fill rate. Both of these procedures were possible only because of the fuel subassembly's simple shape, absence of internal flow passages, and the low decay heat generation. Consequently, it is unlikely that this method could be used on modern-day subassemblies.

The reactions of importance to this process are:

$$Na + H_2O \rightarrow NaOH + 1/2\ H_2 \quad \Delta H^\circ_{(298^\circ K)} = -33.67 \text{ kcal/mole}$$

$$2Na + H_2O \rightarrow Na_2O + H_2 \quad \Delta H^\circ_{(298^\circ K)} = -31.08 \text{ kcal/mole}$$

The advantages of water cleaning are:

1. Economical.
2. Simple.

The disadvantages are:

1. Hydrogen gas evolved is flammable.
2. Overpressurization within restricted flow passages of the subassembly is possible.
3. High temperatures can result from the exothermic reactions if the heat production rate exceeds the removal rate.
4. Corrosion can result, a type of corrosion known as stress corrosion cracking (see Appendix B).
5. Deposits of sodium in pockets or crevices can be covered by sodium hydroxide (caustic) which can retard or even temporarily stop the sodium-water reaction until the sodium hydroxide dissolves. This is called caustic plugging.

Steam mixed with an inert gas such as argon and nitrogen has proven to be a successful subassembly cleaning agent.[7,8,9,10,11] Initially, a mixture of approximately 5% steam and 95% inert gas is circulated through the subassembly. The process is continued with enriched steam, the reaction rate being controlled by the ratio of steam to inert gas. The moist gas technique, or water vapor-inert gas process as it is also called, has been used for Enrico Fermi subassemblies and was the process selected to clean EBR-II fuel subassemblies. To date, the most experience and most favorable results have been obtained with this process. For a detailed description of the water vapor-argon process used at EBR-II, see Appendix A.

The reaction of importance to this process is:

$Na + H_2O \rightarrow NaOH + 1/2\ H_2 \quad \Delta H^\circ_{(298^\circ K)} = -45.7$ kcal/mole

The advantages of steam-inert gas cleaning are:

1. Economical.
2. Limited possibility of overpressure since the reactant fluid is a vapor rather than a liquid.
3. Greater probability of complete reaction since sodium is a liquid at steam temperatures.

The disadvantages are:

1. Hydrogen gas evolved is flammable.
2. Large temperature excursions are possible due to the low heat capacity of steam.
3. Corrosion, particularly stress corrosion cracking (Appendix B) becomes a major concern at elevated temperatures.
4. Difficulty in removing sodium from small cracks and crevices.

Alcohol cleaning is another reactive sodium removal process that has been used at Dounreay, England.[7,8,11,12] In this process, alcohol is allowed to flow through the subassembly and react with the sodium. The reaction rate can be controlled by regulating the alcohol temperature, by choosing the type of alcohol used, or by diluting the alcohol with different molecular weight alcohols, water, or steam. In general, those alcohols with the most carbon atoms per molecule react the slowest. For example, in regard to chemical reactivity:

methanol > ethanol > 1-propanol > 2-propanol, etc., .

A typical reaction between an alcohol and sodium is:

$Na + CH_3OH \rightarrow NaOCH_3 + 1/2H_2 \quad \Delta H^\circ_{(298^\circ K)} = -48.1$ kcal/mole

sodium + an alcohol → an alcoholate + hydrogen

The advantages of alcohol cleaning are:

1. The sodium-alcohol reaction is less rapid than the sodium-water reaction.
2. The latent heat of vaporization of liquid alcohol serves as a reaction rate control. If the reaction is too vigorous, alcohol boils away from the region thereby decreasing the reaction rate.
3. Stress corrosion cracking is essentially eliminated (Appendix B).

The disadvantages are:

1. Alcohol is flammable.
2. Overpressure is possible due to hydrogen evolution.
3. Large quantities of alcohol can be expensive.
4. High temperatures can cause thermal cracking and coking of the alcohol.
5. Some radiolytic decomposition (i.e., coking) of alcohols occurs in high intensity radiation environments.

Ammonia cleaning involves circulating liquid ammonia through the fuel subassembly.[7,8] The characteristic deep blue color of sodium in liquid ammonia serves as a convenient check on the completeness of the cleaning operation.

The advantages of ammonia cleaning are:

1. Ammonia, being a solvent of sodium does not appreciably react chemically at low temperatures, therefore overpressurization due to gas evolution and overheating due to exothermic reactions are not a concern.
2. Negligible corrosion.

The disadvantages are:

1. In order to flush away the sodium, the ammonia must be a liquid. This requires refrigeration equipment or a pressurized reaction vessel. At 70°F, ammonia liquefies at 114 psig.
2. Liquid ammonia is not a solvent for sodium oxide or hydroxide, typical sodium impurities. Ammonium chloride added to the sodium reacts with the sodium oxide to form sodium chloride which is soluble in ammonia, but the ammonium chloride reacts with sodium to release hydrogen.
3. Over long periods of time or at elevated temperatures greater than 300°C (572°F), sodium reacts with ammonia to form sodium amide according to the reaction:

   $$Na + NH_3 \rightarrow NaNH_2 + 1/2\ H_2$$

   The reaction is accelerated by catalytic materials such as iron, copper, zinc, water, oxides, or like materials.

Oil cleaning consists of flushing fuel subassemblies with high temperature and high velocity oil to melt and remove the sodium.[7,8] The Atomic Power Development Associates, Inc. (APDA) conducted a series of tests which produced generally favorable results of cleaning subassemblies with hot oil and ultrasonic agitation.

The advantages of oil cleaning are:

1. Oil does not chemically react with sodium. Consequently, no chemical reactions occur which can lead to overpressure conditions or high temperatures.
2. Oil is dry and therefore prevents water-sodium reactions.
3. Negligible corrosion.

The disadvantages are:

1. Under prolonged high temperatures and radiation conditions, hydrocarbons tend to break down and leave coke deposits.
2. An additional system is required to remove the oil from the subassembly.
3. Expensive.

Vacuum distillation, otherwise known as evaporative cleaning, essentially consists of boiling the sodium from the subassembly surfaces.[7,8] The vapor pressure of sodium at several temperatures is given in Table VI.3.[13] Ongoing research is currently being conducted on this process by the Atomics International Corporation in Canoga Park, California to determine its feasibility.

The advantages of evaporation cleaning are:

1. This process is the most effective in removing sodium, especially from small cracks and crevices.
2. No chemical reactions occur which can lead to overpressurization or high temperatures.
3. Negligible corrosion.

The disadvantages are:

1. At reduced pressures required for lower temperature sodium boiling, the removal of decay heat becomes difficult.
2. A vacuum system is required which may be expensive.

Table VI.3: Boiling Point of Liquid Sodium at Several Pressures.

Pressure (mm of Hg)	Boiling Point (°C)
760	890
400	830
100	700
10	546
1	440

Although most of the results of the sodium removal processes discussed above are based on sodium removal from stainless steel rather than Zircaloy (the exception being the subassemblies at the Enrico Fermi reactor), it is reasonable to assume that these processes would in general be applicable to the removal of sodium from Zircaloy if not other materials as well.

On the basis of the current state of sodium removal technology, the amount of experience gained, and the most favorable results achieved, the water vapor-argon process used at EBR-II is recommended as the process to clean sodium from the Zircaloy clad LWR subassemblies that are removed from the proposed sodium cooled hybrid reactor SOLASE-H. Should the evaporative process prove feasible without damaging subassemblies due to excessive temperatures, this process should be selected over the water vapor-argon process based on the superior cleaning effectiveness of evaporative sodium removal.

APPENDIX A

Water Vapor-Argon Process Used at EBR-II[9,10,11]

The water vapor-argon process (or moist gas process) has been successfully used at EBR-II to remove residual sodium from LMFBR fuel subassemblies. This process removed sodium from exposed surfaces but not from crevices.

After being removed from the reactor, a spent fuel subassembly is allowed to cool for 15 days in the sodium pool of the reactor tank. Then, by means of a Fuel Unloading Machine (FUM), the subassembly is removed from the sodium pool by a grapple which is equipped to direct a stream of argon through it to remove the approximate one kilowatt of fission product decay heat. After a delay to permit drainage of sodium from the surface of the subassembly, it is drawn completely into the fuel unloading machine where pure argon is circulated through it at approximately 30 cfm. The FUM then travels on rails to transfer the subassembly into the interbuilding transfer cask. This 20 ton, portable, lead shielded cask[14] (Figure 1) transfers fuel subassemblies to and from the reactor and adjoining Fuel Cycle Facility (FCF) where subassemblies are dismantled and the fuel removed. The cleaning operation to remove the normal residual sodium coating of between 20 to 40 grams is performed within this cask.

The water vapor-argon sodium removal process is initiated by introducing humidified air (air bubbled through water) at a rate of 0.4 cfm to the recirculating argon coolant. The amount of water and air available for the oxidation of the sodium is increased gradually because the recirculating cooling argon (30 cfm) is removed at a rate of 0.4 cfm. The reactor rate is monitored by a thermocouple in the reaction chamber so as to maintain the temperature below 300°F (149°C).

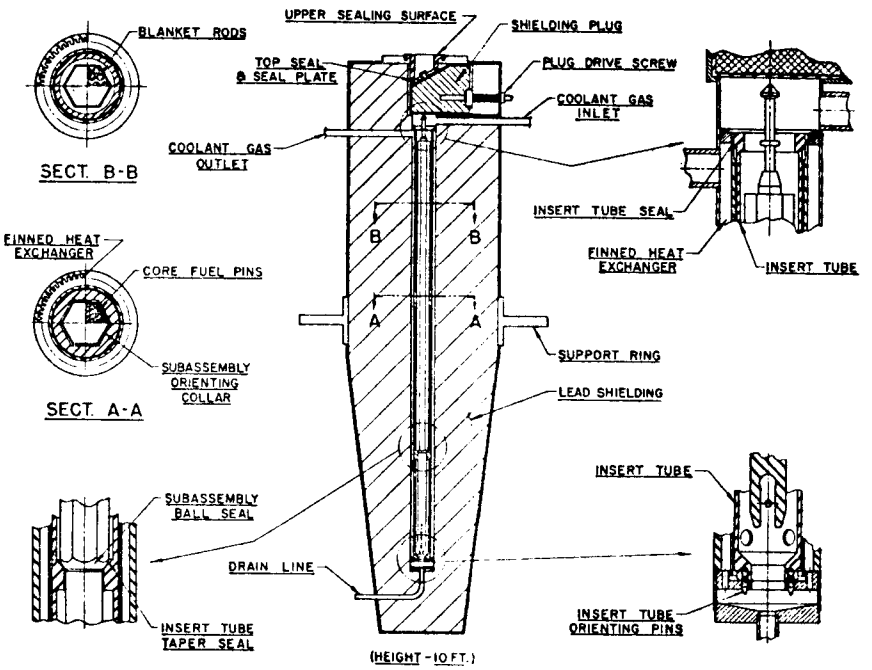

Figure 1a: Fuel transfer cask, internal construction.

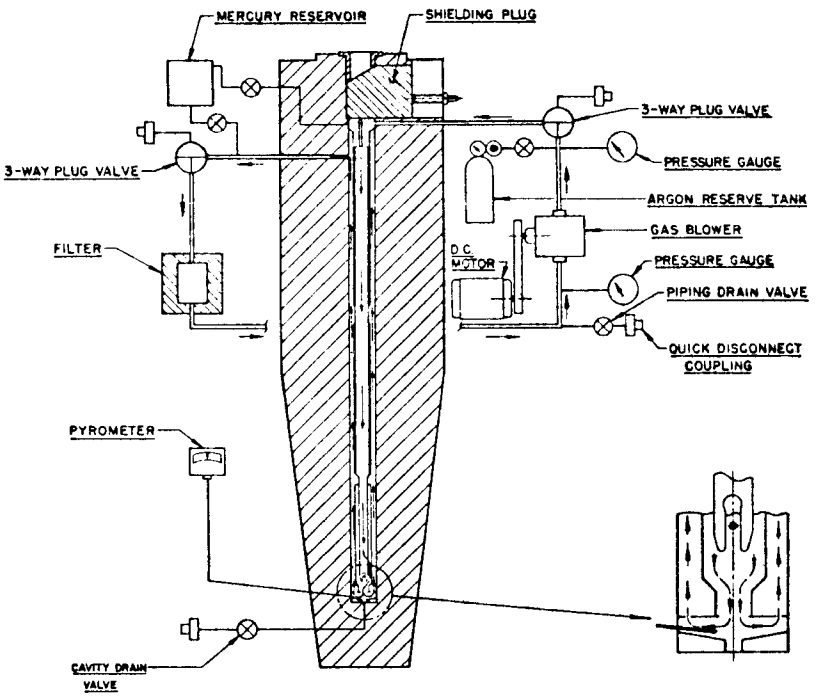

Figure 1b: Fuel transfer cask, gas circulation system.

After 15 minutes of humidified air flow at 0.4 cfm, the flow of the humidified air is increased to 7 cfm and maintained at that level for 15 minutes. At the end of this period, the flows of humidified air and recirculating argon are stopped and the subassembly is rinsed by flowing purified water up through it at a rate of 5 gpm. Twenty-five gallons of water are used to rinse a normal driver fuel subassembly. The subassembly is then dried by passing dry air through it at a rate of 30 cfm for 60 minutes, purged, recirculated with argon, and a fission gas sample is taken to detect failed fuel.

Experimental subassemblies are subjected to a similar operation except that humidified argon only (no air) is used. The 0.4 cfm flow of moist argon is maintained for 60 minutes and the 7 cfm flow is maintained for 30 minutes. The subassemblies are rinsed until samples of the effluent rinse have a conductivity less than 0.8 micromho and a sodium content less than 0.4 ppm.

APPENDIX B

Stress Corrosion Cracking[11]

When a metal is stressed, stress concentrations result near the tips of any cracks or crevices in the material. As a result the chemical potential, or equivalently the strain energy density of the metal, increases in the region of the stress concentration. If the crack is filled with an electrolytic solution, effectively, the stress concentration region becomes anodic while the rest of the metal becomes cathodic. Consequently, enhanced dissolutioning occurs at the tip of the crack resulting in the propagation of the crack. This process is referred to as stress corrosion cracking.

In the water vapor-inert gas sodium removal process, the reaction product, sodium hydroxide (caustic) produced from the reaction,

$$Na + H_2O \rightarrow NaOH + 1/2H_2$$

is an ionic compound which dissociates in solution to form the electrolyte required for stress corrosion cracking to occur. On the other hand, in an alcohol cleaning process, which can be represented by the reaction,

$$Na + ROH \rightarrow RONa + 1/2H_2$$

sodium → an alcohol → an alcoholate → hydrogen;

a non-ionic alcoholate is formed. The resulting nonelectrolytic organic solution therefore does not promote stress corrosion cracking.

Much of the development of the moist gas technique has been concerned with developing process conditions that will avoid corrosion damage to the components being cleaned. The results of this work are summarized in

Figure 2. This chart has been successfully used as a guide in assessing the degree of component safety associated with specific processing conditions. No stress corrosion cracking has been observed in EBR-II fuel subassemblies subjected to the water vapor-argon technique described in Appendix A.

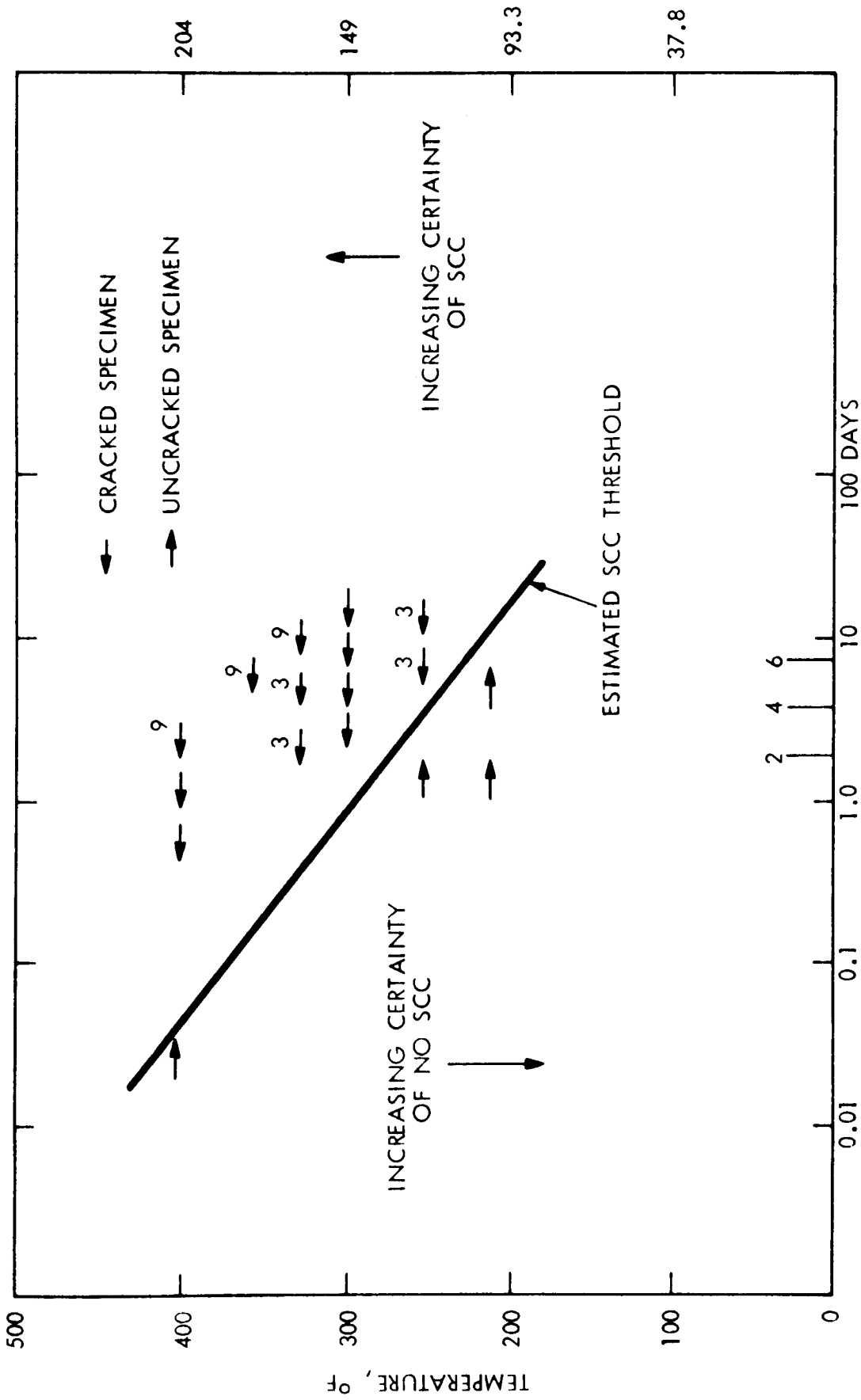

Figure 2: Times in days to when SCC was observed in 50 wt% NaOH-water solution sleeved 304 stainless steel tensile specimens stressed to 100% of 0.2% offset yield.

References for Section VI

1. George Leslie Miller, Zirconium, 2nd ed., (New York: Academic Press Inc., 1957).

2. "Zirconium in the Nuclear Industry," Proceedings of the Third International Conference ASTM, (1976).

3. M. Davis and A. Draycott, "Compatibility of Reactor Materials in Flowing Sodium," Proceedings of the Second United Nations International Conference on the Peaceful Uses of Atomic Energy, Vol. 7 (1958).

4. Warren E. Barry, Corrosion in Nuclear Applications (New York: John Wiley and Sons, 1971).

5. J.C. Bokros, Effect of Sodium on Mechanical Properties of Zirconium, NAA-SR-1867 (Atomics International, 1957).

6. R.L. Carter, R.L. Eichelberger, and S. Siegel, "Recent Developments in the Technology of Sodium-Graphite Reactor Materials," Proceedings of the Second United Nations International Conference on the Peaceful Uses of Atomic Energy, Vol. 7 (1958).

7. John G. Yevick, Fast Reactor Technology: Plant Design (Massachusetts: M.I.T. Press, 1966).

8. O.J. Foust, Sodium-NaK Engineering Handbook, Vol. 3, (New York: Gordon and Breach, Science Publishers, Inc., 1978).

9. R.A. Cushman, W.H. Perry, and J.I. Sackett, "Cooling of Experimental Subassemblies During Removal from the EBR-II Reactor," The Winter Annual Meeting of the American Society of Mechanical Engineers, Vol. 2 (1971).

10. R.V. Strain, "Effects of Sodium and Sodium Removal on the Microstructure of Type 304 Stainless Steel Tubing," EBR-II Project (1969).

11. RDT Standard: Sodium Removal Processes, RDT-F-S-9T (Oak Ridge, Tennessee: Oak Ridge National Laboratory, 1977).

12. F.H. Welch, O.P. Steele, III, "Sodium Technology: The Reaction Rates of Sodium with Alcohols," Rockwell International, Atomics International Division (1977).

13. CRC Handbook of Applied Engineering Science, 2nd Edition, (1976), 337.

14. G.J. Bernstein, A.A. Chilenskas, and R.F. Malecha, "Interbuilding Fuel Transfer Coffin for the EBR-II Reactor," (Argonne, Illinois: Argonne National Laboratory, 1964).